The Torque Magnetometry Study of Underdoped $YBa_2Cu_3O_y$

by

Fan Yu

A dissertation submitted in partial fulfillment
of the requirements for the degree of
Doctor of Philosophy
(Physics)
in The University of Michigan
2017

Doctoral Committee:

Associate Professor Lu Li, Chair
Assistant Professor Xiaogan Liang
Professor Vanessa Sih
Associate Professor Kai Sun
Assistant Professor Liuyan Zhao

Fan Yu

fanyuchn@umich.edu

ORCID iD: 0000-0002-1762-6072

Acknowledgements

I would like to thank my advisor Prof. Lu Li for his support. Prof. Li is very knowledgeable, and his leading-by-example is the most beneficiary for his students. Though very busy and often under pressure, Prof. Li made sure that he would have time to chat with and assist his students. I feel so fortunate to have Prof. Li as my advisor.

Dr. Gang Li, who was post-doctoral researcher in Prof. Li's group, generously offered his help in my training and my research projects. The other group members, including Ben Lawson, Colin Tinsman, Ziji Xiang and Lu Chen, are also very helpful in many aspects.

During my study, I visited National High Magnetic Field Laboratory (NHMFL) many times. NHMFL provided world-class experimental facilities. Many research scientists I met there provided great assistance to our experiments. They are Dr. Singleton, Dr. Balakirev, Dr. Betts, Dr. Zapf, Timothy Murphy, Dr. Ju-Hyun Park and others.

During the process of my defense, the committee members kindly pointed out the deficiencies and offered valuable suggestions.

Finally, I owe my gratitude to my families.

Contents

List of Figures

List of Tables

Abstract

This thesis describes torque magnetometry study on under-doped $YBa_2Cu_3O_y$. Torque magnetometry measures the anisotropic magnetization of materials, and is among the most sensitive experimental methods to probe superconducting state. This study's motivation is to apply this method to the open question: how much does the superconducting fluctuations persist into the pseudogap region, where various ordered states are observed?

Experiments at temperatures close to and above T_c was conducted. Diamagnetic component was extracted from the samples' observed magnetization. The result was in agreement with the theory as well as previous study on different underdoped superconducting cuprates. These evidence indicates that the superconducting fluctuations persist deeply into the pseudogap region (quantitative detail see Chapter.3).

Furthermore, torque magnetometry was successfully conducted with superconducting samples with T_c ~62 K, at temperatures one order of magnitude lower than T_c and DC magnetic field upto 45 Tesla. Before this, torque magnetometry experiment on underdoped cuprates was never conducted so deeply inside the superconducting dome. A "kink" feature, shown as abnormal behavior in magnetization and more clearly revealed as a peak in differentiated susceptibility dM/dB, was observed at temperatures below 40 K, once the superconducting state with long range coherence was suppressed by strong magnetic field.

The "kink" feature has either a two dimensional or highly anisotropic origin along the ab-plane, and demonstrated very weak temperature dependence. Comparisons with results by thermal conductivity, X-ray scattering, nuclear magnetic resonance (NMR) and ultrasonic methods were made. Apparently, the "kink" feature shows up on phase diagram in the same region where the charge density wave (CDW) transi-

tion was known to exist. Thus, it is suspected that the "kink" feature is originated from the superconducting fluctuations influenced by a CDW related transition.

The observation of the "kink" feature, combined with results on diamagnetism and our collaborators' results on thermal conductivity, we are able to rule out a previous estimation of H_{c2} that is misleadingly low in magnetic field and/or temperature.

Finally, efforts to extend torque magnetometry method to pulsed magnetic field were introduced. Since the highest available DC magnetic field is limited to 45 Tesla, AC magnetic field which could reach 65 Tesla is the only choice for experiments aimed at the deeper parts of the superconducting dome. The situations and their unique challenges, as well as our preliminary results were analyzed in detail.

Chapter 1

Introduction

High temperature superconductivity in perovskite-structured copper oxides (cuprates) is a huge topic. This chapter will provide a review of the literature upto ∼year 2013, when I started my torque magnetometry project on the under-doped $YBa_2Cu_3O_y$ (YBCO).

Furthermore, this chapter will also explain the motivation behind this project. Specifically, it will answer the following questions: 1st, why would we focus our study at a sample with hole doping level $p \sim 0.11$? 2nd, why would we use an experimental method that is highly sensitive to the superconducting state while not sensitive to the spin/charge order state?

1.1 High Temperature superconductivity in Cuprates

The high temperature superconductivity in perovskite-structured copper oxides (cuprates) has inspired huge amounts of studies since its discovery in 1986 by Bednorz and Muller[2]. This is driven not only by the desire of finding compounds of higher critical temperatures T_c[31, 3], but also by numerous experimental observations indicating that high temperature superconductivity rises out of a very different physics process.

Finding high temperature superconductivity in a transition-metal oxide is itself a rather unexpected result. The parent compounds of this type of high T_c superconductors are Mott insulator[21] with layered structures. Mott insulator is a material which should be metallic according to band theory, but is insulating due to strong electron-electron repulsion (particularly in low temperatures). In this case, in the undoped material, the copper ion in the Cu-O layer has a single hole

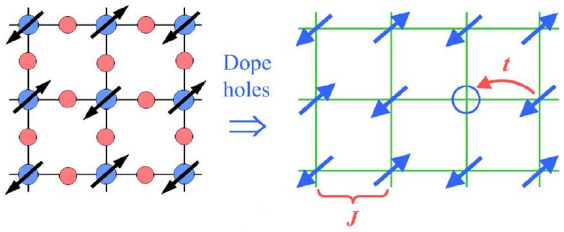

Figure 1.1: Two dimensional Cu-O layer (left). Simplifying to the one-band model after hole doping (right). Adapted from [17].

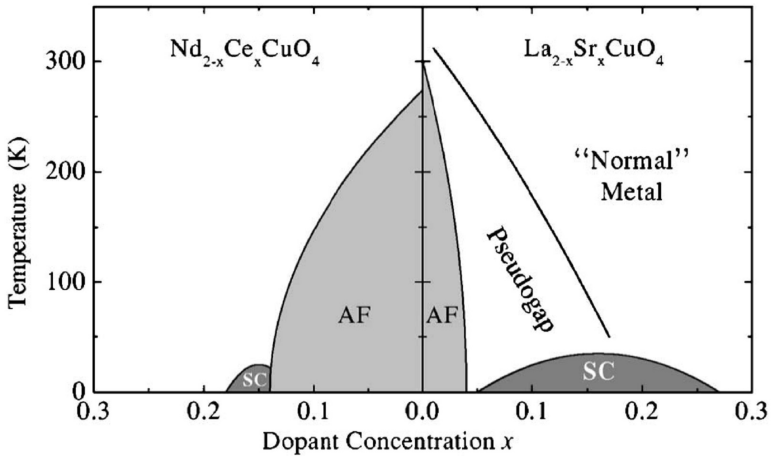

Figure 1.2: Schematic phase diagram of high-T_c superconductors with hole doping (right) and electron doping (left). Adapted from [17].

per unit cell. According to conventional band theory, this compound should be metallic as its band is half-filled. However, due to strong correlation effects, the repulsive energy cost (commonly called U) when putting two electrons (or holes) on the same ion dominates the hopping energy t, making the ground state an insulator. Furthermore, neighboring spins in the copper-oxygen layer would be anti-aligned due to energy considerations caused by virtual hopping. Thus this Mott insulator should also demonstrate antiferromagnetism. However, as shown in Fig.1.2 superconductivity would emerge at the expense of antiferromagnetism when extra holes or electrons are added to the Cu-O layer.

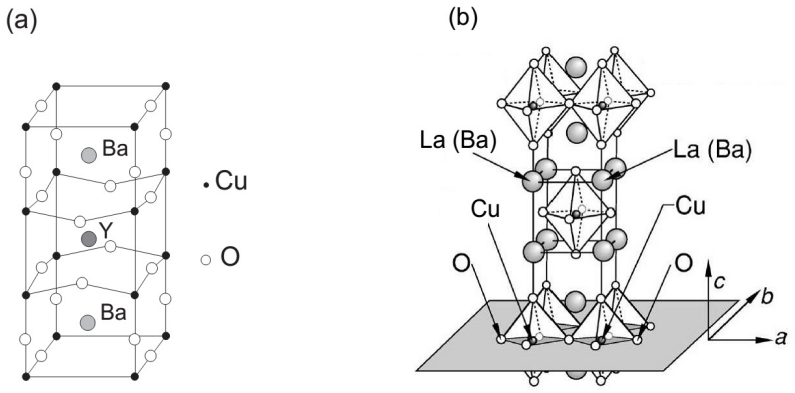

Figure 1.3: Two dimensional Cu-O layer (left). Simplifying to the one-band model after hole doping (right). Adapted from [17].

The compound under study in this thesis - $YBa_2Cu_3O_{6.55}$ - belongs to a large family of high-T_c compounds sharing a layered structure of copper-oxygen planes. The square-like Cu-O plane could be seen in Fig.1.3, where the spacing between Cu ions is about $3.78 \sim 3.88$. This type of compounds could be further divided into two subgroups: the 214-system based on $La(Nd,Pr)_2CuO_4$ and the 123-system based on $YBa_2Cu_3O_6$. Structurally, the two systems are different. For the 123-system, there is one Y-O layer and two Ba-O layers between the Cu-O planes, with four Cu-O chains along the c-axis. These Cu-O chains serve as "charge reservoirs" and determine the carrier concentration in the Cu-O planes. If there is oxygen deficiencies in the Cu-O chains, which could be generated by sample annealing treatments, negative charge will be drained from the Cu-O planes. Effectively, holes are added into the Cu-O planes. By contrast, there is no Ch-O chains in the 214-system. Take the $La_{2-x}Ba_xCuO_4$ for example. There are two layers of La(Ba)-O planes between Cu-O planes. Since Ba will attract negative charges from the Cu-O planes, the hole concentration level in $La_{2-x}Ba_xCuO_4$ is controlled by Ba doping, which is called hole doping. Similarly, electron doping is also possible, for example, Ce doping in $Nd_{2-x}Ce_xCuO_4$.

1.2 The Pseudogap Phase

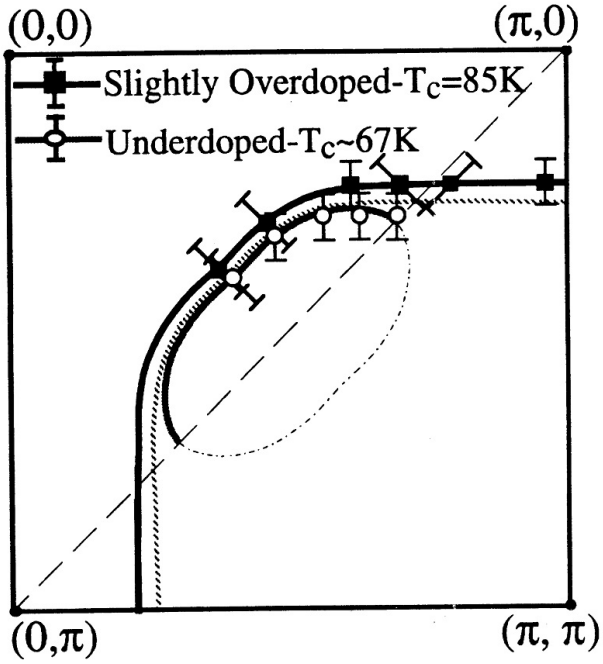

Figure 1.4: Fermi surface in Bi2212. The Fermi surface of the under-doped sample is an open arc while that of over-doped sample is closed. Adapted from [20].

Fig.1.2 is a schematic phase diagram of 214-system at zero magnetic field.[1] Starting from the undoped material, the ferromagnetic dome collapses rapidly with increasing hole doping level. The superconducting state emerges out of the end of antiferromagnetism dome. The critical temperature T_c of the superconducting phase reaches its maximum at the optimal doping. The region in the phase diagram where doping level is lower than the optimal doping is called the under-doped region. As indicated in Fig.1.2, the region above the under-doped superconducting dome is called pseudogap region, where the material does not behave as a normal Fermi

[1] In the hole doped side of the phase diagram, 123-system and 214-system is qualitatively very similar.

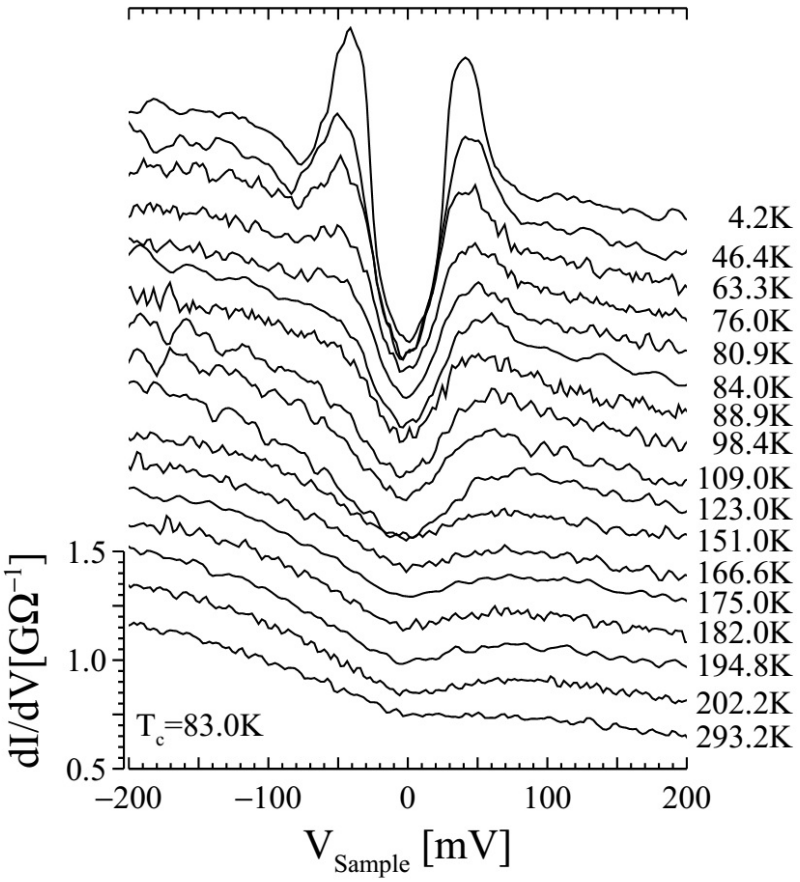

Figure 1.5: Tunneling conductance for under-doped Bi2112. Adapted from [22].

liquid metal.

This part of the phase diagram is called pseudogap region because of the growth of a pseudogap at the Fermi surface[26], which could be understood as scenario where only some regions of the Fermi surface become gapped. As illustrated in Fig.1.4 by early studies[20], the Fermi surface of under-doped cuprates is qualitatively different from that of over-doped cuprates. The changed of Fermi surface depending on doping level will be discussed in sections below. Various experimental methods, including angle resolved photoemission, tunneling spectroscopy, nuclear magnetic resonance, transport measurement, have been applied to study this region. One of

the most revealing results could be seen in Fig.1.5 using tunneling spectroscopy[22], where one could observe two symmetrically placed conductance peaks on both sides of the zero bias conductivity depression, representing the gap, below the critical temperature T_c. However, when temperature is raised through T_c, one didn't see a sudden close of this gap; instead, it persists onto much higher temperatures.

Finally, I would like to point out that the pseudogap region exists in the under-doped hole side of both 123-system and 214-system. It is not, however, revealed in the under-doped electron side of the 214-system. This may due to the fact that the antiferromagnetism is the electron-doping side is stronger and partially overlaps with the superconducting dome.

1.3 Fermi Surface Reconstruction and Quantum Critical Points

$YBCO_y$	p (holes/Cu)	T_C(K)
$YBCO_{6.45}$	0.078	44.5
$YBCO_{6.48}$ II	0.083	49.5
$YBCO_{6.48}$ III	0.085	51.0
$YBCO_{6.48}$ I	0.088	53.0
$YBCO_{6.51}$	0.097	57.3
$YBCO_{6.54}$	0.108	61.3
$YBCO_{6.67}$	0.120	66.0
$YBCO_{6.75}$	0.132	74.8
$YBCO_{6.80}$	0.135	77.9
$YBCO_{6.86}$	0.152	91.1

Table 1.1: Relations between the hole doping level per planar Cu ion, the oxygen content y and the superconducting transition temperature in zero magnetic field.

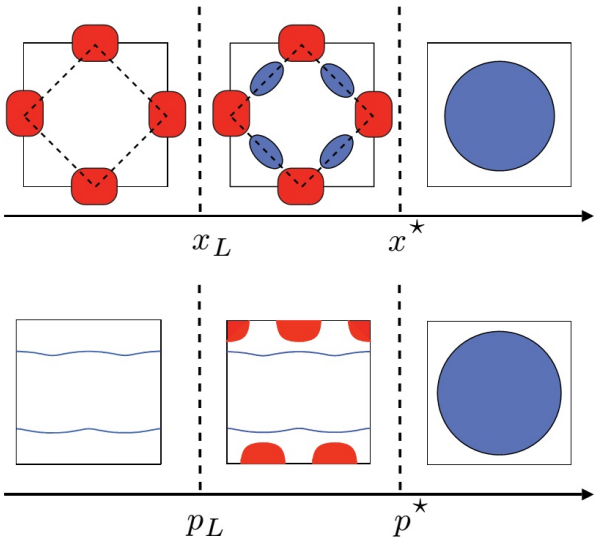

Figure 1.6: Schematics of Fermi surface reconstruction in cuprates. Upper panel is the electron doping case, lower panel is the hole doping case. Adapted from [15].

The existence of a small closed Fermi pocket, in addition to the open Fermi surface arc shown in Fig.1.4, was first revealed by studies of quantum oscillations of the hole-doped 123-system in the under-doped region[6, 13, 24]. Experiments in similar doping levels yielded a negative Hall coefficient[14], indicating that the close Fermi pocket is electron-like rather than hole-like, as one would expect from a hole-doped system. This small closed electron-like Fermi pocket in under-doped region is qualitatively different from the large hole-like cylindrical Fermi surface in the over-doped region[28]. Thus one would expect a transition of the Fermi surface as a function of doping level p, which is often called Fermi surface reconstruction. The doping level that separates these two different metallic states is designated as p^*. Furthermore, later experiments on Hall coefficient indicates that the electron-like Fermi pocket disappears in the deep under-doped region[15], indicating a second transition point which is designated $p_L \sim 0.08$, as shown in Fig.1.7. In the literature, p^* and p_L are often called quantum critical point(s) since the Fermi surface

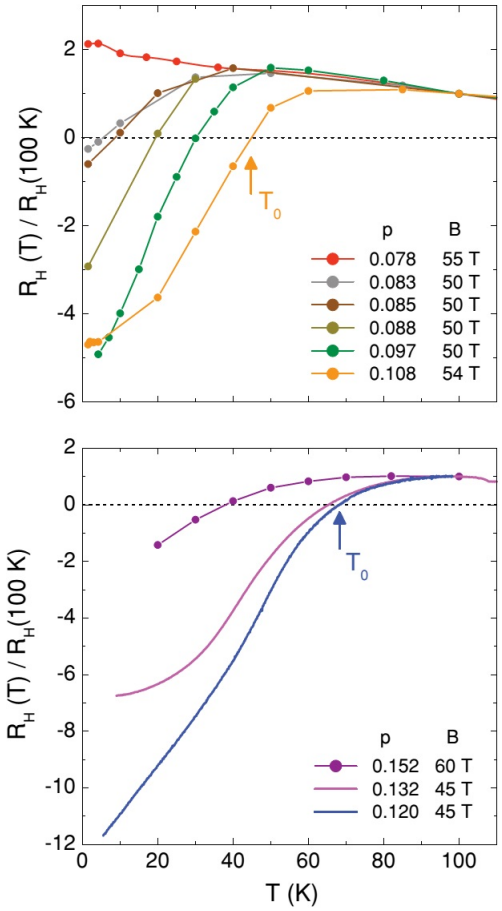

Figure 1.7: Hall coefficient of YBCO at different dopings level, normalized to its value at $T = 100K$. Adapted from [15].

reconstruction is believed to happen at the T=0 limit and in the absence of superconducting state. Although there is evidence that quantum oscillation from the electron-like Fermi pocket persists into the vortex solid state of the superconducting phase at low temperature, direct evidence for the T=0 limit is hard to come by.

The evolution of Fermi surface as a function of doping level p is schematically illustrated in Fig.1.6, where blue(red) region indicates hole(electron)-like Fermi pockets while blue line indicates hole-like open Fermi arc. The behavior of Fermi surface for the electron-doped side is similar; a pair of critical doping levels x^* and x_L

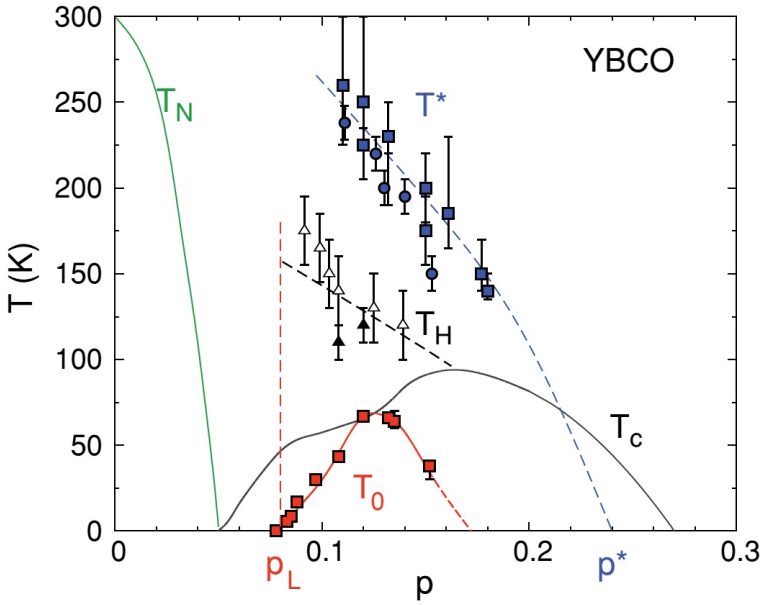

Figure 1.8: Phase Diagram of $YBa_2Cu_3O_{6+\delta}$. p is the hole doping level per planar Cu ion. Adapted from [15].

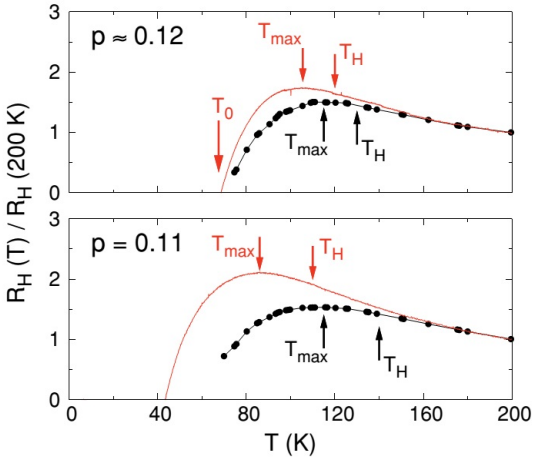

Figure 1.9: Temperature dependence of R_H, normalized to its value at 200K. Adapted from [15].

could be defined in the same way. The qualitatively similar evolution of Fermi surfaces on both sides of the anti-ferromagnetic (AFM) dome indicates that the

Fermi surface reconstruction is closely related to orders originating from the AFM state. For the sample under study, under-doped YBCO, the order causing Fermi surface reconstruction is believed to be the unidirectional spin density wave (SDW) order, often called stripe order, which breaks both the translational symmetry and the rotational symmetry of the CuO_2 planes. Evidences supporting this argument includes: anisotropy of the in-plane resistivity[1], neutron scattering[11] and microwave conductivity[10].

The Fermi surface reconstruction and the quantum critical points are also closely associated with the pseudogap region. Fig.1.8 is the phase diagram of $YBa_2Cu_3O_{6+\delta}$ at zero magnetic field. T_N is the antiferromagnetic ordering temperature. This $T_N \sim 300K$ at zero hole doping level is relatively low; and there is significant antiferromagnetic fluctuations at temperature higher than T_N. With increasing hole doping level, the superconducting state emerges out of the end of antiferromagnetism dome. The critical temperature T_C of the superconducting phase reaches its maximum at the optimal doping $p = 0.15$. T^* is defined as the temperature below which the resistivity (blue circles) and the Nernst coefficient (blue squares) deviate from their high-temperature behavior. It is believed that a k-dependent scattering mechanism emerges around T^*, causing deviation in resistivity and Nernst signal, thus could be taken an approximate upper boundary of the pseudogap region. T_H is defined as the point where Hall coefficient starts the downward turn[15] while T_0 is defined as the point where Hall coefficient crosses zero. T_H is believed to be the temperature where the electron-like pocket emerges due to a broken translational sysmmetry. T_H and T_0 could be more figuratively understood in Fig.1.9. The red dashed line marks the critical doping $p_L = 0.08$ below which Hall coefficient no longer demonstrates a downward turn with decreasing temperature.

It is worth noting that, in the study of various abnormal phenomenons in the pseudogap region, a broad, gradual transition like the one in Fig1.8 and Fig.1.9 is

more often encountered than a sharp, clear-cut one. This is partially due to different experimental methods are sensitive towards different physics processes. For example, quantum oscillation measurements in conductance and magnetization channels are blocked by the superconducting state in low temperature, but heat capacity measurement[23] could extend measurement of Fermi surface into the vortex solid state.

1.4 The Competing Orders

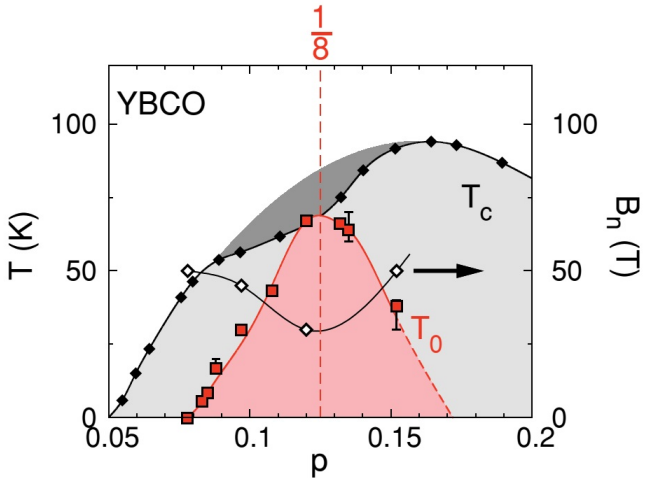

Figure 1.10: Phase diagram of hole-doped YBCO zoomed in around $p \sim 1/8$. Adapted from [15].

As argued in Section.1.2 and Section.1.3, the pseudogap region is interesting not only because it has many different states, but also because there is no clear boundaries between these states. One understanding is that these states are competing in nature.

A good example is the dent of the T_c curve around $p \sim 1/8$ (see Fig.1.8). This dent or plateau of T_c is due to competition between superconducting states and the

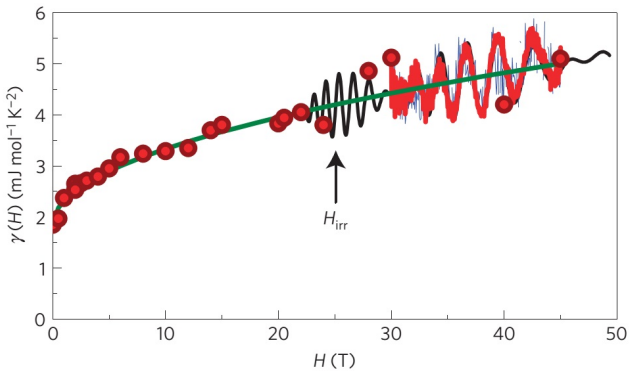

Figure 1.11: $\gamma(H) = C(T, H)/T$ for YBCO 6.56. Adapted from [23].

stripe order[2]. The latter were more stable at $p \sim 1/8$ due to commensurate locking with the lattice[15].

In Fig.1.10, the shaded area above T_c curve is the expected superconducting dome if the under-doped side was to be symmetrical with the over-doped side. The curve connecting white diamonds is the resistive upper critical field B_n, which could be taken the point where magnetic field kills the long range coherence of superconducting state. Thus B_n characterizes the strength of superconducting state. The curve connecting red squares is the sign-change temperature T_0 of Hall coefficient, representing a characteristic temperature where the electron-like Fermi pocket dominates the transport signal. The most revealing feature in Fig.1.10 is that both the B_n curve and the T_0 curve are symmetric around $p \sim 1/8$, indicating the superconducting order and the stripe order are connected and competing with each other.

As argued in previous Section.1.3, the Fermi surface reconstruction is caused by the symmetry breaking stripe order. In the literature, due to the experimental challenges of suppressing the superconducting state at zero temperature limit, the metallic state one would observe after suppressing the superconducting state

[2]a form of spin density wave (SDW).

at finite temperature is also called the magnetic-field induced resistive state. One experiment study[23] of the Fermi surface reconstruction was conducted by S. C. Riggs using heat capacity method. As argued by the author, heat capacity method has the unique strength that it "probes the nature of all low-energy excitations continuously across H_{irr}", the boundary of the vortex solid state, below which transport and magnetization methods are not effective. Thus, if the stripe order does not compete with superconducting state and exists deep inside the superconducting dome, then one should expect an early onset of quantum oscillation signals. However, this is not the case. By Fig.1.11, one could see the onset of quantum oscillation lies shallowly H_{irr}, indicating a competing relation.

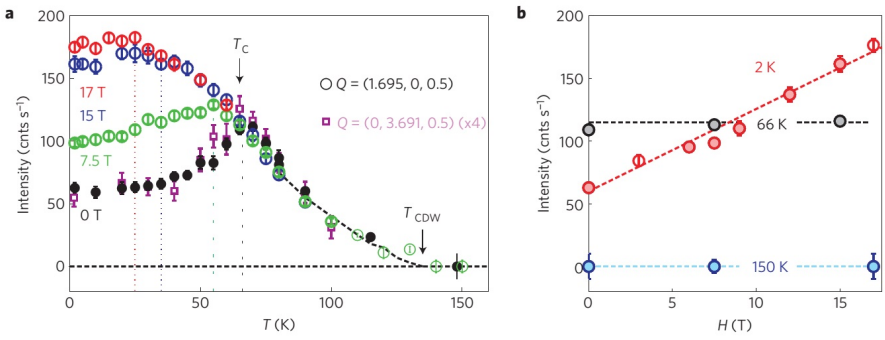

Figure 1.12: Panel a: Temperature dependence of the peak intensity at (1.695, 0, 0.5) as circles and (0, 3.691, 0.5) as squares (scaled) for different applied magnetic fields. Panel b: Magnetic field dependence of the peak intensity at (1.695, 0, 0.5) for different temperatures. Adapted from [4].

More recently, additional charge order was observed in YBCO using NMR[32], x-ray diffraction[7, 4] and ultrasonic[16] methods. This charge order is a static modulation of charge density in the CuO_2 planes of $YBa_2Cu_3O_y$. Like the stripe order, the charge order also breaks translational symmetry.

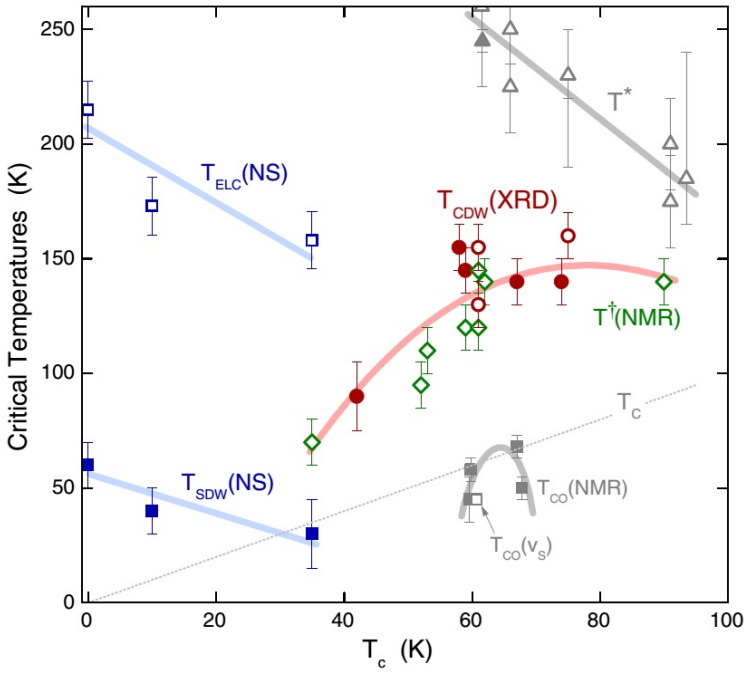

Figure 1.13: Phase diagram of YBCO. Plotting against T_c removes ambiguities of how doping level p is determined. Adapted from [12].

Fig.1.12 is one of the most revealing experimental evidence supporting the competing relation between superconducting state and the charge order state. A sharp decrease of peak intensity reflecting weakened charge order at T_c could be observed when applied magnetic field is small or non-exist. Furthermore, peak intensity at fixed low temperature increases monotonously when the superconducting state is weakened by applied magnetic field. Please note that at 2K, 17 Tesla is not sufficient to kill the long range coherence of superconducting state. In other words, the 2K data of panel b are taken when both states coexists. The charge order is often called "magnetic field induced" in the literature. However, similar to the case of Fermi surface reconstruction, this only illustrates the experimental necessity of using high magnetic field to suppress the superconducting state so that the hidden states could be observed.

Finally I would like to point out that, there is also competing relation between the spin order and the charge order in the deep under-doped region. However, that would not be a focus of this thesis.

Now we are in a position to answer the question: why would we focus our study at a sample with hole doping level $p \sim 0.11$? This particular doping level is within the pseudogap region, it is between the two critical doping levels (p^* and p_L) where the electron-like Fermi pocket exists, it is close to the $p \sim 1/8$ dent on the superconducting dome where the stripe order is strongest due to commensurate locking, and by Fig.1.13, it is also close to the doping level where the charge order is strongest[3]. In short, this is an ideal doping level to study interactions between various orders in the under-doped cuprate YBCO.

1.5 Vortex Liquid State

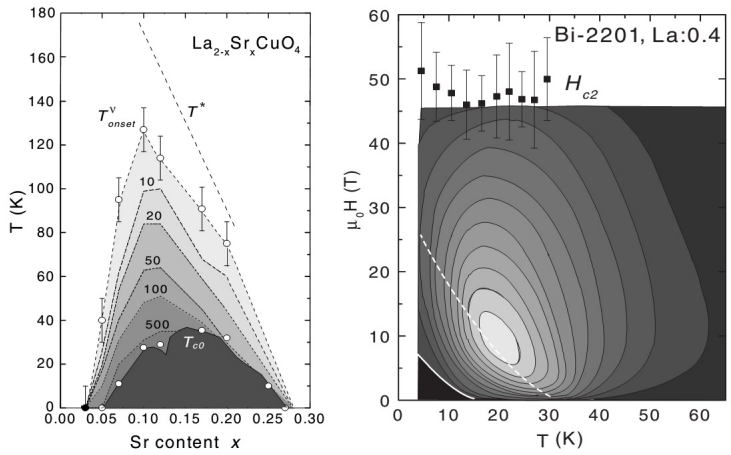

Figure 1.14: Phase diagram based on Nernst measurement in the pseudogap region, from under-doped 214-system. Adapted from [30].

[3]Although different experiment methods yield different results, they are indicating a maximum onset temperature at $p \sim 0.11$.

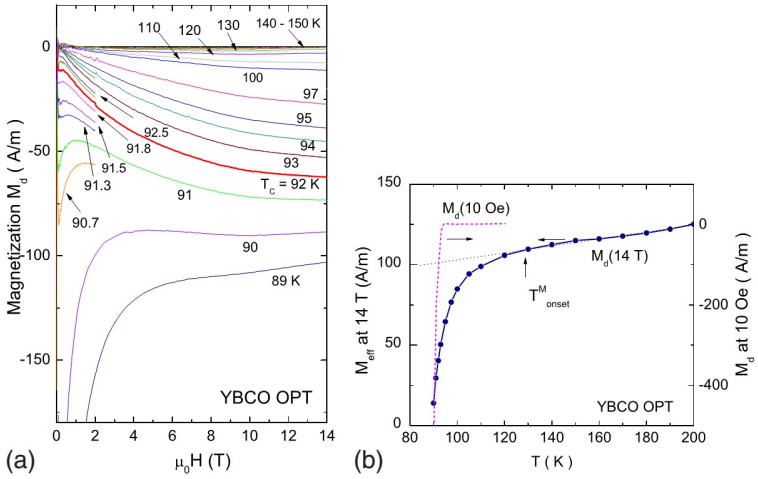

Figure 1.15: Panel a: diamagnetism of YBCO $p \sim 0.15$. Panel b: Temperature dependence of observed magnetization M_{eff} at 14 Tesla. Adapted from [19].

In Section.1.2, the pseudogap phase was introduced as a scenario that the superconducting gap persists into higher temperatures after Copper pair density lost its long range coherence. In Section.1.3 and Section.1.4, a picture of competing orders was introduced, where suppression of the superconducting state is necessary to reveal the reconstructed Fermi surface and the charge order state. Thus, it is argued that a lower estimation of H_{c2} close to the boundary of vortex solid state[4] would be expected for the superconducting state.

However, experiments using the Nernst method[30] and the torque magnetometry method[19] indicate that the superconducting state persists into much higher temperatures, in the form of vortex liquid phase. Vortex liquid phase is characterized by short-range superconducting correlation, with the long-range coherence degraded by vortex motion. In the Nernst method, vortex liquid state is detected when the vortexes are driven into motion by the temperature gradient and generating the Josephson voltage pulses. In the torque magnetometry method, vortex

[4]The boundary of vortex solid state is also where T_c and H_{irr} are defined.

liquid state is detected by the comparatively strong diamagnetic signal from the "short-range Meissner effect" around the cores of remaining vortexes.

The question regarding upper critical field H_{c2} is further compounded by the fact that contradicting arguments were based on experimental methods that have different sensitivity towards various phases in the pseudogap region. Methods like NMR[32], x-ray diffraction[7, 4] and ultrasonic[16] are very sensitive to symmetry breaking orders, and were the main experimental methods making direct observation of the ordered states. However, they could only provided indirect measurements regarding the existence of superconducting states. Thus it is necessary to supplement existing arguments with results from torque magnetometry, which is very sensitive to and measures directly the superconducting state. This answers the question: why would we use an experimental method that is highly sensitive to the superconducting state while not sensitive to the spin/charge order state?

In previous magnetometry studies of under-doped YBCO shown in Fig.1.15, the temperature range was kept close to and above T_c. This is mainly due to the rapid increasing of H_{irr} in lower temperatures. However, it is necessary to conduct experiments in lower temperatures in order to observe pseudogap phases. This created conflicting requirements for the torque magnetometry setup. On one hand, detecting potential signatures due to the ordered states in higher magnetic fields on the magnetization channel would require high sensitivity, because this is indirect measurement and the signatures are expected to be small. On the other hand, the torque system needs to survive the hysteresis in lower magnetic fields before vortex solid state is suppressed. This demands large dynamic range. How to solve this problem will be explained in the Chapter.2.

1.6 Organization

This thesis will be organized as follows: Chapter.2 offers a short introduction on DC magnetometry experiment methods; Chapter.3 will present the main DC magnetic field results of torque magnetometry study on $YBa_2Cu_3O_{6.55}$; Chapter.4 will discuss my efforts of extending capacitive torque magnetometry method into pulsed magnetic field experiment.

Chapter 2

Introduction to Torque-Magnetometry

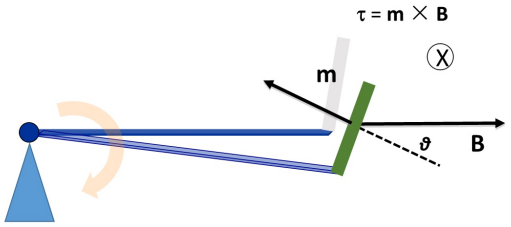

Figure 2.1: Schematic of torque-magnetometry measurement.

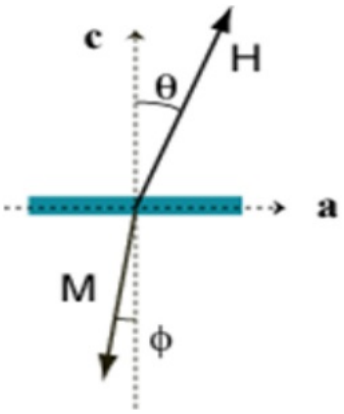

Figure 2.2: Schematic of the dominantly diamagnetic scenario.

Torque-magnetometry method is an experimental method that is sensitive to magnetic anisotropy. As shown in Fig.2.1, the torque generated exerted on the cantilever could be expressed as:

$$\tau_{t,b} = \frac{1}{2} H_z^2 (\chi_{aa} - \chi_{cc}) sin2\theta - H_z^2 \chi_{ac} cos2\theta \tag{2.1}$$

Usually, the χ_{ac} termed could be ignored. Even so, compared with other methods like vibrating sample magnetometer (VSM) or SQUID which measure only χ_{cc}, the torque-magnetometry method would rely on further restrictions on the properties of the sample to have a direct interpretation of the data.

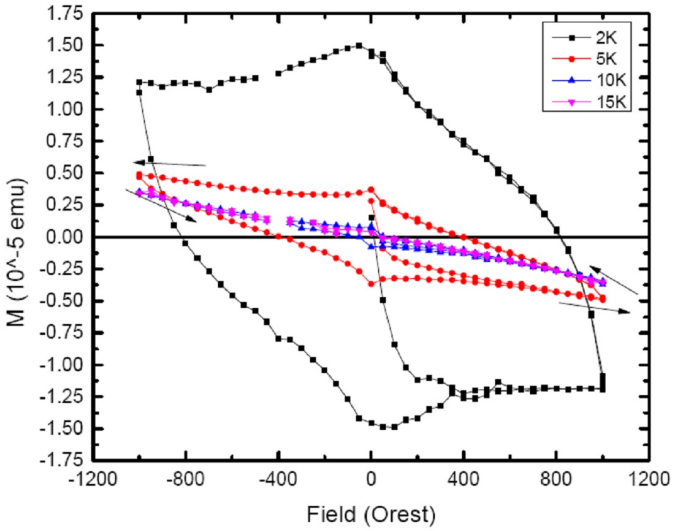

Figure 2.3: PPMS measurement of χ_{cc} for sample $[(Li_{1-x}Fe_x)OH](Fe_{1-y}Li_y)Se$.

In our study of cuprates, due to the semi-2D property of the sample, when the temperature is below or close to the critical temperature T_c, the signal we obtained through torque-magnetometry could roughly be taken as a good approximation to the signal induced by external magnetic field along the c-axis.

However, in a previous study on $[(Li_{1-x}Fe_x)OH](Fe_{1-y}Li_y)Se$, where there is both superconducting component (along the c-axis) and ferromagnetic component (in the ab-plane), the interpretation of the data is much more complicated. As in Fig.2.3, one could clearly observe a standard hysteresis loop behavior from the superconducting states by using a method sensitive only to χ_{cc}. However, in Fig.2.4, torque-magnetometry yields a heavily distorted hysteresis loop that closes and reopens multiple times with increasing magnetic field. This is because the superconduct-

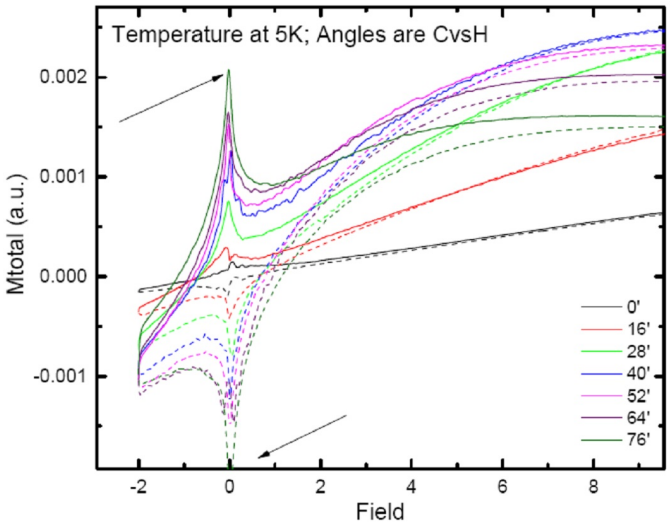

Figure 2.4: Torque-magnetometry measurement of $[(Li_{1-x}Fe_x)OH](Fe_{1-y}Li_y)Se$. The signal comes from a combined dependence of χ_{cc} and χ_{aa} on external magnetic field.

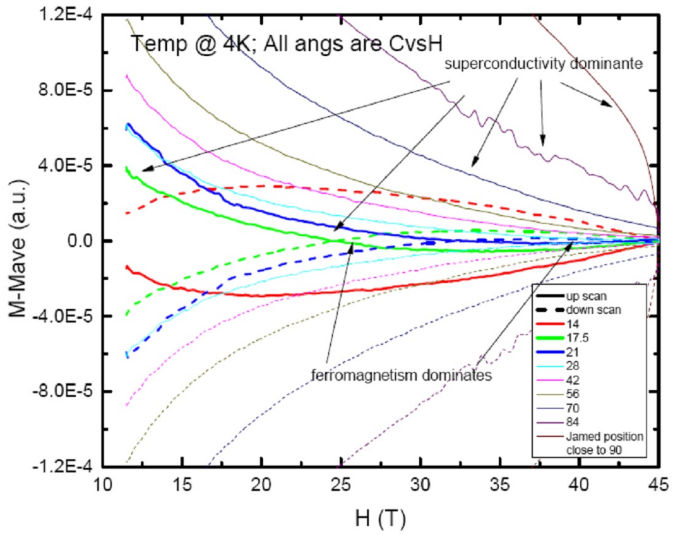

Figure 2.5: Torque-magnetometry measurement of $[(Li_{1-x}Fe_x)OH](Fe_{1-y}Li_y)Se$, in a higher magnetic field comparable to H_c of the ferromagnetic state in ab-plane.

ing state and ferromagnetic state in $[(Li_{1-x}Fe_x)OH](Fe_{1-y}Li_y)Se$ are of comparable strength under $\sim$5 K temperature, thus the first term in Equ.2.1 could not be

simplified.

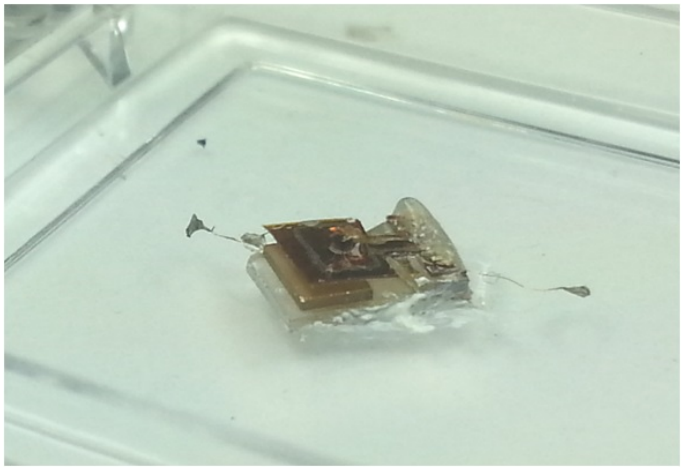

Figure 2.6: Cantilever made of 3-mil kapton. $YBa_2Cu_3O_{6.55}$ mounted with ab-plane perpendicular to the cantilever head.

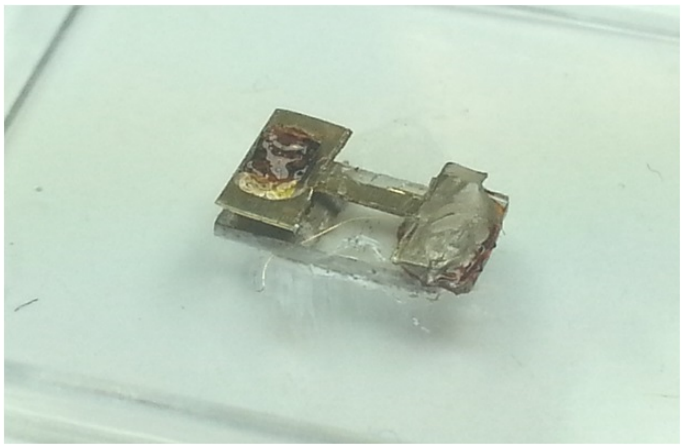

Figure 2.7: Cantilever made of 3-mil brass. $YBa_2Cu_3O_{6.55}$ mounted with ab-plane parallel to the cantilever head.

The cantilever devices we used for this study are shown in Fig.2.6 and Fig.2.7. Cantilevers are made of either brass or kapton with the underside coated with aluminum. Directly below the cantilever head is a piece of sapphire or quartz

coated with gold, thus creating a parallel capacitor between the two. The parallel capacitor formed by the cantilever head and the coated sapphire or quartz below is usually on the order of $\sim$0.3 picofarad (pF), which is called C_0. The linear range of such is roughly 10% of C_0. The sensitivity of the cantilever is directly related to the stiffness of the "neck", which is controlled by choosing different material and different geometry. A correct choice could yield a device reaching 10^{-9} emu sensitivity easily.

A major experimental challenge is how to handle the conflict between achieving a higher sensitivity and maintaining the device in the linear range, since the former requires a weaker "neck" while the latter a stronger one. This problem is particularly acute for this project because the signal from the superconducting hysteresis loop is two to three orders of magnitude stronger than that from the "normal state", once the superconducting state is suppressed.

There are also other minor challenges, for example, how to prevent the sample from flying off or breaking apart under extreme conditions. As shown in the pictures, the sample is mounted with silver epoxy in the bottom, to prevent it from falling off the cantilever; then the sample is wrapped with multiple layers of thin GE varnish, to prevent the sample from fracturing under tensions generated by the high magnetic field.

Chapter 3

Magnetometry Study of $YBa_2Cu_3O_{6.55}$

This chapter will present the main DC magnetic field results of torque magnetometry study on $YBa_2Cu_3O_{6.55}$. Section.3.1 will discuss how diamagnetic component is separated from the magnetometry signal; Section.3.2 will discuss the features we observed after separation, particularly the "kink" feature; Section.3.3 will discuss boundaries of the vortex solid state and de Hass van Alphen oscillation; Section.3.4 will discuss the vortex liquid state; Section.3.5 will discuss in-depth the "kink" feature and compare it with results from other experimental methods.

3.1 Magnetization Component Separation

Previously, a comprehensive study [19] has been performed on the under-doped 214-system. Here we adopt a similar method of separating different magnetization components.

The "observed" magnetization M_{obs} is defined and calculated as

$$M_{obs} = \tau/(V\mu_0 H \sin\theta) \tag{3.1}$$

where τ is the torque signal estimated using cantilever's spring constant and observed change in capacitance ΔC, V is the sample volume and θ is the tilt-angle between sample's c-axis and applied magnetic field H. Depending on temperature, M_{obs} could be separated into two parts: a diamagnetic contribution from superconducting state $M_d(T, H_z)$ and a contribution from an-isotropic susceptibility $\Delta\chi_p H_z$.

$$M_{obs} = M_d(T, H_z) + \Delta\chi_p(T) H_z \tag{3.2}$$

where $\Delta\chi_p(T) = \chi_c(T) - \chi_{plane}(T)$, where $\chi_i(T) = \chi_i^v + \chi_i^s(T)$. χ_i^v is the Van Vleck (orbital) susceptibility and $\chi_i^s(T)$ is the spin susceptibility.

The spin susceptibility $\chi_i^s(T)$ has significant temperature dependence. In a previous study[18], an oscillatory behavior in magnetization due to $\chi_i^s(T)$ was observed in deeply under-doped $La_{2-x}Sr_xCuO_4$ with x smaller than the critical doping level $x_L \sim 0.055$ in sub-Kelvin temperature range. For our experiment, the doping level p is much larger than p_L and the lowest temperature data used for claims relating to magnetization is $\sim 3.25K$. Thus it is safe to assume that $\chi_i^s(T)$ is weakly anisotropic and could be dropped from $\Delta\chi_p(T)$.[1]

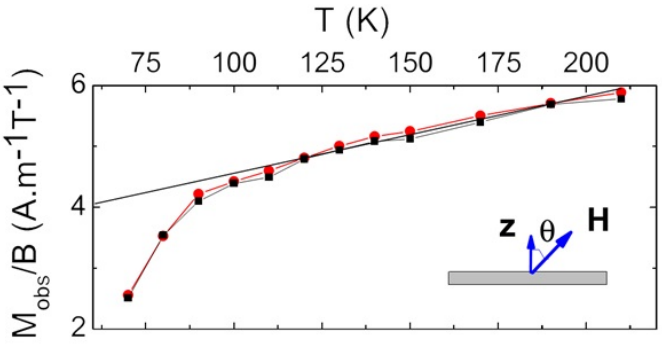

Figure 3.1: Linear temperature dependence of the observed magnetism M_{obs}.

On the other hand, the Van Vleck term χ_i^v is strongly anisotropic but has a linear temperature dependence which could be modeled as

$$\Delta\chi^v(T) = a(T + T_0) \tag{3.3}$$

When temperature is sufficiently higher than T_C, contribution from superconducting state $M_d(T, H_z)$ does not exist, linear fitting to a temperature dependent data set

[1]Please note that, in Fig.3.2, the spin term ΔM_s saturates quickly with increasing magnetic field. The saturation point also towards lower magnetic field when temperature decreases. These are all favorable behaviors for my experiment.

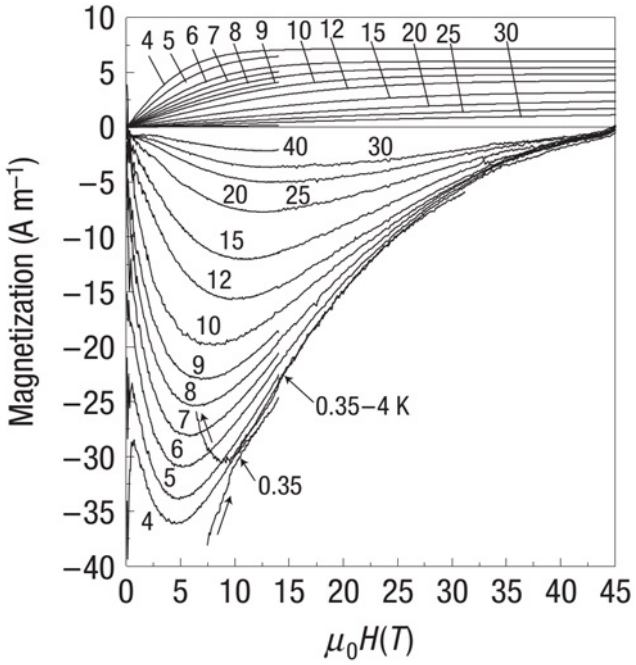

Figure 3.2: Diamagnetic term M_d(negative) and spin term ΔM_s(positive) of LSCO with $T_c \sim 5K$. Adapted from[18].

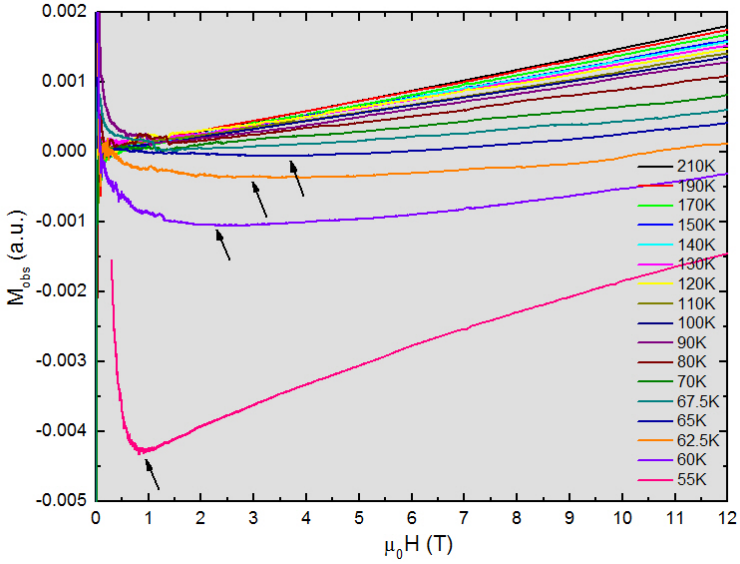

Figure 3.3: M_{obs} of $YBa_2Cu_3O_{6.55}$.

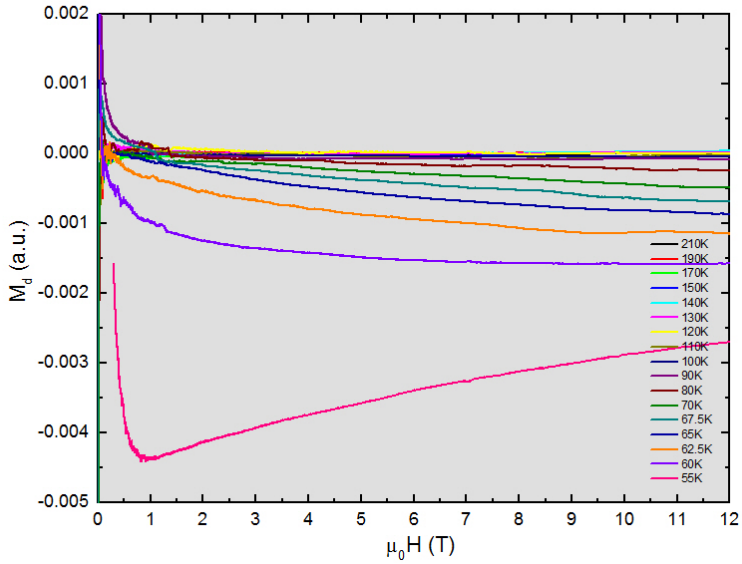

Figure 3.4: M_d of $YBa_2Cu_3O_{6.55}$.

would yield $a = 1.18 \times 10^{-2} A(mTK)^{-1}$ and $T_0 = 305$ K, as shown in Fig.3.1. These constants could be used to obtain $M_d(T, H_z)$ by subtracting the Van Vleck term from M_{obs}.

$$M_d(T, H) = M_{obs}(T, H) - a(T + T_0)H \tag{3.4}$$

Fig.3.3 shows the observed magnetism M_{obs} plotted against magnetic field. Fig.3.4 shows the diamagnetic contribution M_d from superconducting state plotted against magnetic field.

3.2 Diamagnetism of $YBa_2Cu_3O_{6.55}$

The study of diamagnetism was conducted on three samples on three different fridge-magnet systems. Data for Fig.3.4 was taken on sample NO.3 which was only used for estimating the a and T_0 constants. Experiment conducted with Janis fridge and 18 Tesla magnet. Since a and T_0 does not depend on properties of cantilever nor sample volume, they could be used to analyzed data from other samples. Sample

NO.1 and sample NO.2 were used in the 35 Tesla resistive magnet system and the 45 Tesla hybrid system. Sample NO.1 was also used in the pulsed magnetic experiments.

As will be argued in Section.3.4, results by Fig.3.4 was sufficient make the argument that short-range, local fluctuation of superconducting state persists into a much higher region in the magnetic field - temperature phase diagram. It is safe to argue that, at temperatures close to $T_c \sim 62K$, fluctuating superconducting states persists to at least 18 Tesla.

At temperatures below T_c, diamagnetic signal strengthens rapidly. Left hand side of Fig.3.5 is the observed magnetism M_{obs}. For temperature range 10$\sim$40 K, the M_{obs} remains negative after melting field H_m[2] to 20$\sim$30 Tesla, without subtracting the Van Vleck term. Right hand side of Fig.3.5 shows the post-subtraction results, indicating diamagnetic signal persists to at least 35 Tesla. Compared with previous work on 214-system cuprates[18], the key difference is that this study of the vortex liquid state is conducted at temperatures more than one order of magnitude smaller than T_c, after suppressing superconducting states using strong magnetic field. Although several other works also reached this condition , torque-magnetometry has the advantage as the most direct and sensitive method to superconducting states.

From right hand side of Fig.3.5, it is clear that in the magnetic field range 15 24 Tesla, temperature range 10 20 K, there is a turning point on the M_d curve, in the sense that concave/convex property of the curves changed. This feature could be more clearly observed by taking the 1st derivative of M_d, as indicated in Fig.3.6 and Fig.3.7. We call this feature "kink" feature because it is represented as a peak rising above the differential susceptibility, defined as $\frac{\partial M_d}{\partial H_z}$. H_K is defined as the

[2] H_m is defined as the point where hysteresis closes, which is the boundary of vortex solid state.

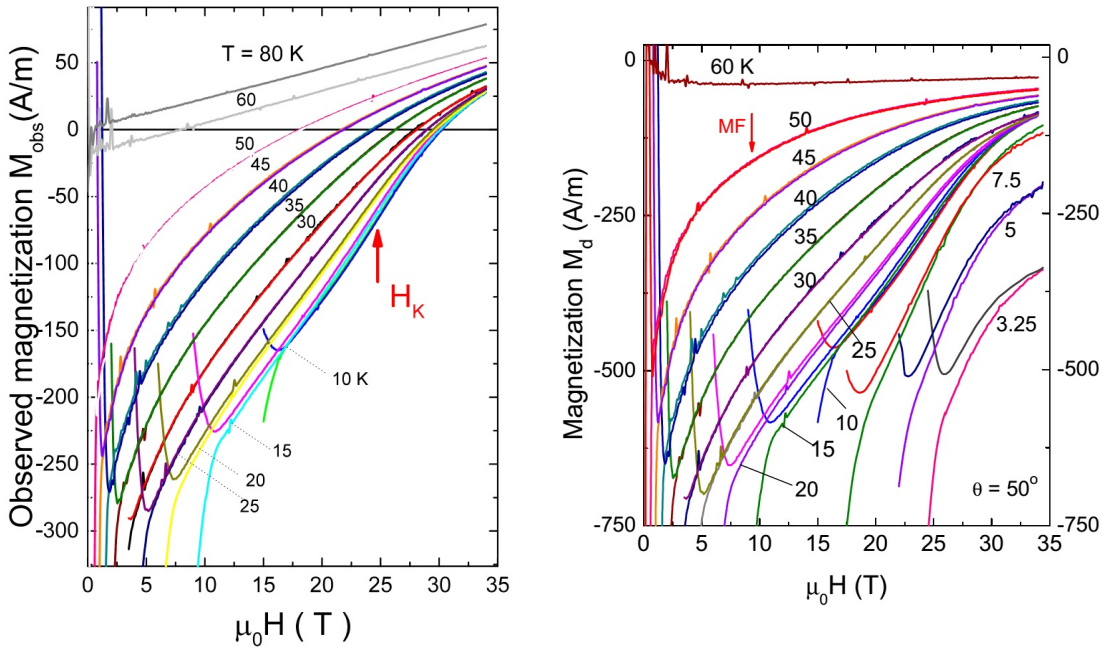

Figure 3.5: Left-hand side: M_{obs} of $YBa_2Cu_3O_{6.55}$. Right-hand side: M_{obs} of $YBa_2Cu_3O_{6.55}$.

characteristic magnetic field where this feature arises.

As could be seen from Fig.3.6, this "kink" feature demonstrated a strong $1/cos\theta$ dependence on magnetic field H, where θ is the angle between sample c-axis and magnetic field H. This indicates that the physics mechanism behind this "kink" feature is strongly confined to the ab-plane. Although there is no direct evidence that the feature originates from the CuO plane, yet most pseudogap phases observed in this part of the phase diagram are two dimensional with the ab-plane. Since this "kink" feature is observed on the magnetization channel, combined with its two dimensional behavior, it is most likely that the "kink" feature is connected to the fluctuating superconducting state of $YBa_2Cu_3O_{6.55}$ in the vortex liquid region.

Interestingly, by Fig.3.7, the position of H_K demonstrates only a week temperature dependence while the "kink" peak on the $\frac{\partial M_d}{\partial H_z}$ curve sharpens rapidly with

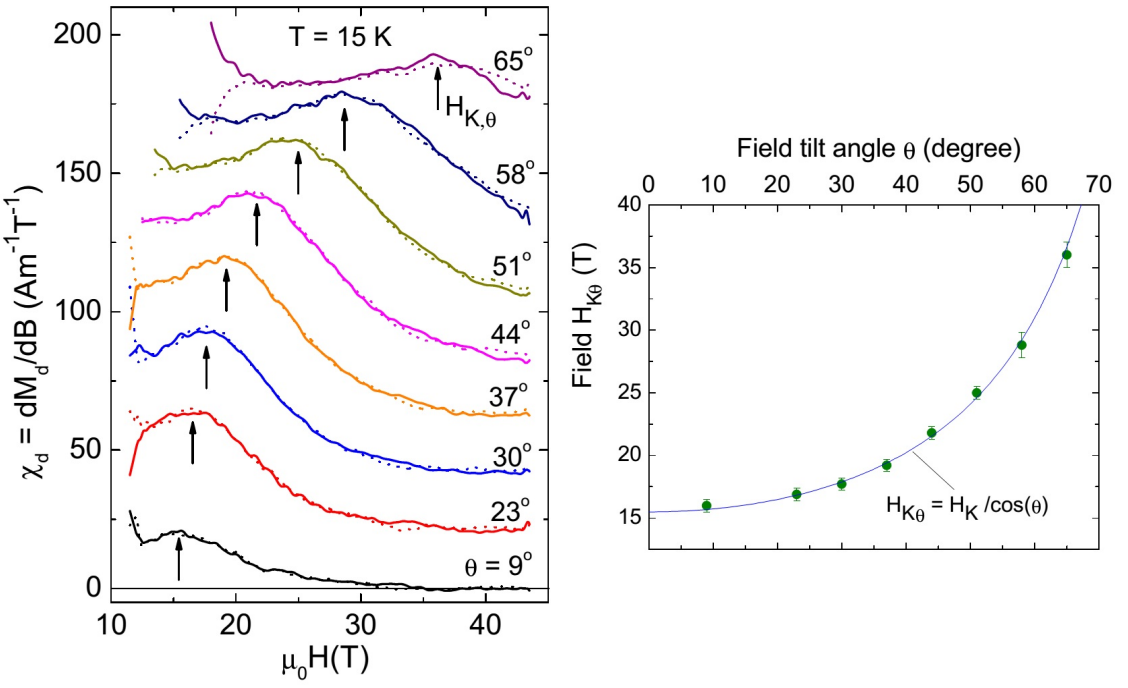

Figure 3.6: Left-hand side: 1st order derivative of M_d, $\frac{\partial M_d}{\partial H_z}$, at different angles. Right-hand side: a clear $1/cos\theta$ dependence on magnetic field H_z.

decreasing temperature. This observation creates complications in understanding the origin of this feature.

On one hand, the fact that this "kink" feature is observed in the magnetization channel and that it demonstrated a clear $1/cos\theta$ angular dependence[3] indicates that this feature is associated with the fluctuating superconducting state. Particularly, by Fig.3.5, the shift of M_{obs} caused by the "kink" feature is on the order of tens of A/m within ~10 Tesla, which is too strong to be produced by other sources. Finally, both the Van Vleck term and the spin term only have a monotonous dependence on magnetic field.

On the other hand, this "kink" feature is unlikely to be associated with the vortex solid state of the superconducting phase. Vortex solid state expands rapidly into

[3]This angular dependence rules out possibilities from defects or impurities of the sample.

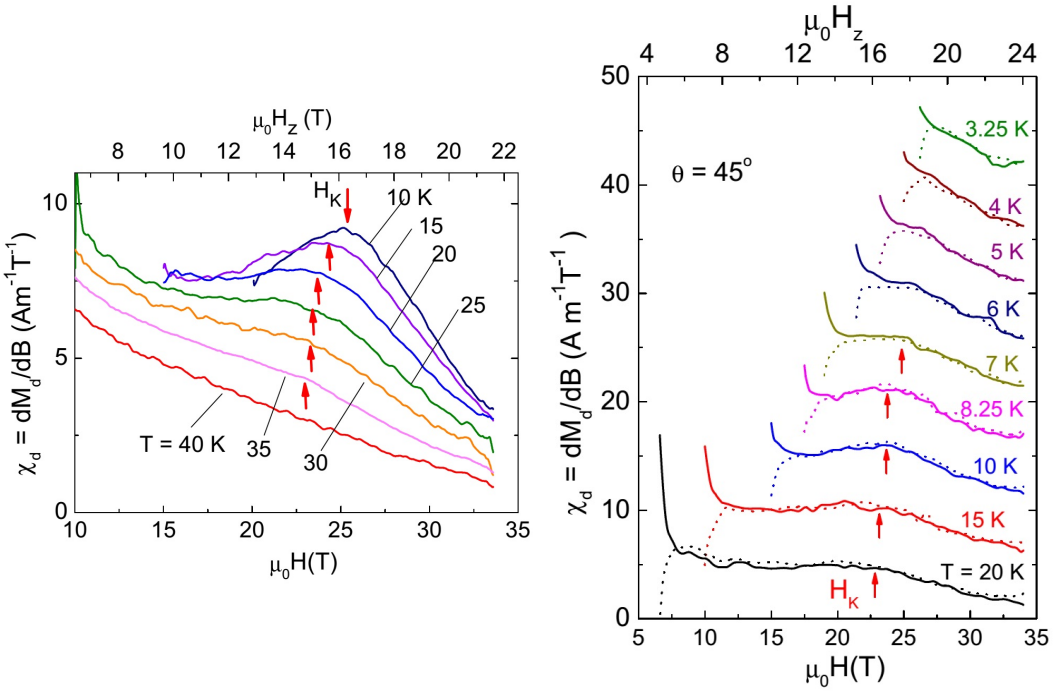

Figure 3.7: 1st order derivative of M_d, $\frac{\partial M_d}{\partial H_z}$, at different temperatures.

higher magnetic field with decreasing temperature, one would expect H_K moving to higher magnetic field along with H_m. However, right-hand side of Fig.3.7 indicates that with decreasing temperatures, the "kink" feature is suppressed by the hysteresis of superconducting vortex solid. Thus torque-magnetometry along would not be able to determine issue, but some other experimental methods indicate that this feature do persist into vortex solid state.

To fully understand this almost temperature independent feature, one has to look at results from other experimental methods, particularly results on other ordered states in the pseudogap region.

To summarize, at temperatures below T_C, fluctuating superconducting state persists into at least 35 Tesla after suppressing the vortex solid state using high magnetic field. Furthermore, a "kink" feature is observed above the melting field H_m at a characteristic field H_k. H_k demonstrates $1/cos\theta$ angular dependence and very

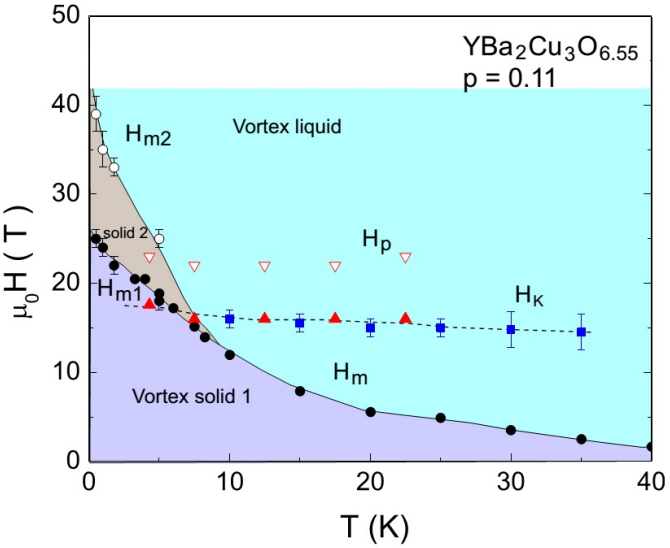

Figure 3.8: Phase Diagram drawn from our torque-magnetometry data and our collaborators' thermal conductivity data.

weak temperature dependence. Nonetheless, the "kink" feature itself becomes more prominent at lower temperatures. This could be summarized into the phase diagram as in Fig.3.8.

3.3 Discussion: H_m and Quantum Oscillation

As argued in Chapter.1, many pseudogap phases was observed only when the vortex solid state is suppressed by magnetic field. Thus it is important to know its precise boundary H_m[4], which could be estimated by observing the closing point of hysteresis loop of sample magnetization using torque magnetometry method. H_m could be reliably established for temperatures above 10K. For lower temperatures, the situation is complicated.

[4]Sometime also called H_{irr}

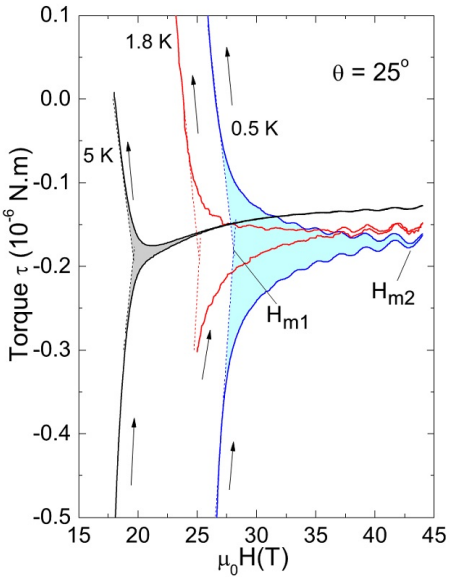

Figure 3.9: Low temperature measurement on sample NO.2 mounted on brass cantilever. The trumpet like region following the hysteresis (which could not be seen in this plot) was mistaken as evidence of vortex solid 2.

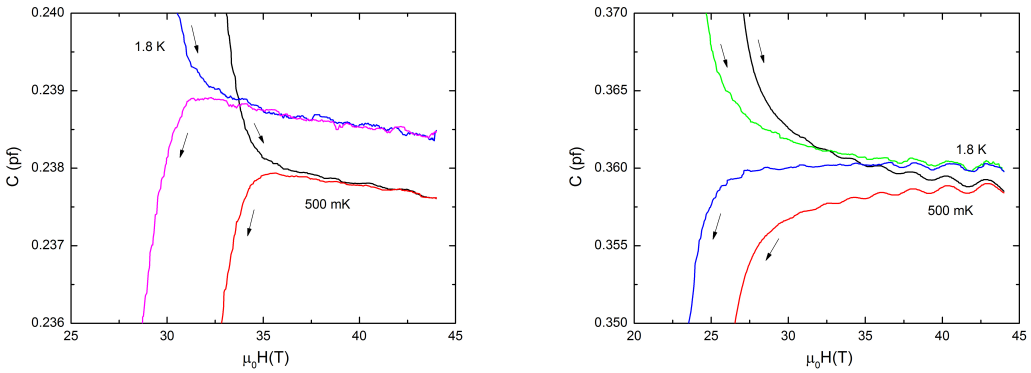

Figure 3.10: Left-hand side: dC measurement on sample NO.1 mounted on kapton cantilever. Angle between c-axis and magnetic field $\theta \sim 47$ degree. Right-hand side: dC measurement on sample NO.2 mounted on brass cantilever. $\theta \sim 25$ degree.

In our original paper[34], we argued that the superconducting state adjusts to the appearance of three-dimensional charge density wave (CDW) in the form of a sharp change in shear moduli. Thus the vortex solid state in low temperatures should be

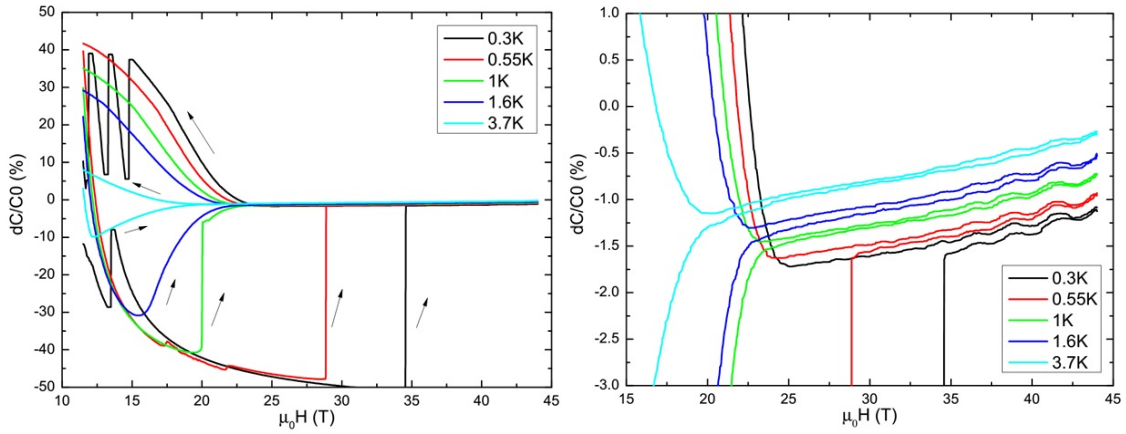

Figure 3.11: Left-hand side: dC/C_0 measurement on sample NO.1 mounted on kapton cantilever. Right-hand side: zoom-in of left hand side. For temperatures below 5K, the magnitude of signal beyond H_m is much smaller than the hysteresis.

separated into two parts[5], with the boundary of vortex solid 2 rising much faster with decreasing temperature, as shown in Fig.3.8 and Fig.3.9.

However, this argument is most likely wrong. First, Fig.3.9 is taken from sample NO.2, which is much larger in volume compared with sample NO.1. And it is mounted on a brass cantilever, which is prone to deformation. Fig.3.10 is a comparison of sample NO.1 and NO.2. From left hand side of Fig.3.10, the smaller sample NO.1 mounted on kapton cantilever[6] doesn't demonstrate the extensive trumpet like behavior as that of the right hand side. Second, H_m from left hand side of Fig.3.10 would be 23.9T while H_{m1} from right hand side would be 27.2T. These estimations are very close. Third, although sample NO.1 mounted on kapton cantilever also has non-overlapping traces as in Fig.**??**, they are of different shape and much smaller than the hysteresis.

Furthermore, we obtained quasiparticle parameters using de Hass van Alphen oscillations observed in temperatures below 5K, shown in Fig.3.12. Panel a and b

[5]Vortex solid 1 has larger shear moduli than vortex solid 2.

[6]Kapton cantilever is more flexible, has larger dynamic range compared with brass cantilever.

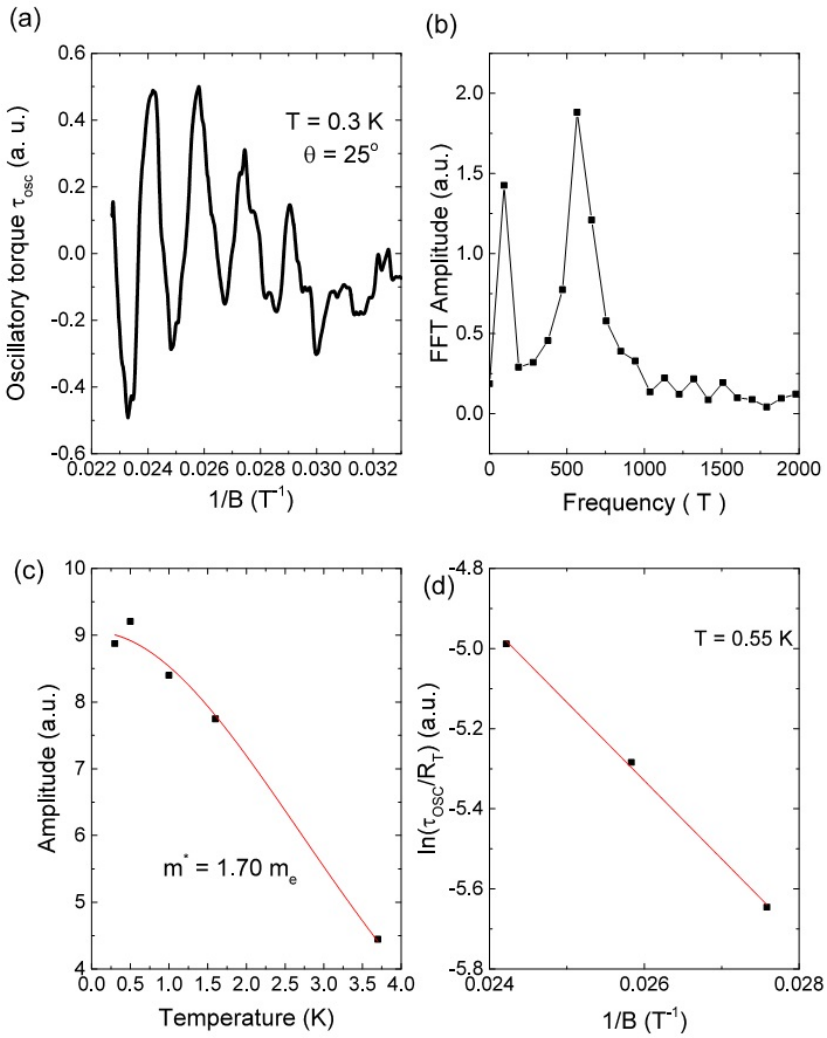

Figure 3.12: Panel a: the oscillatory component of the torque τ_{osc} vs. $1/H$ for the sweep-down trace in sample NO.2 at 0.3K. Panel b: the fourier spectrum of τ_{osc} obtained by FFT analysis, yielding a strong peak at 560T. Panel c: amplitude of τ_{osc} measured at $H = 30$T versus Temperature. We obtain an effective mass $m^* \sim 1.70m_e$. Panel d: the Dingle plot of the oscillation amplitude vs. 1/B measured at 0.55K. We obtain the Dingle temperature ∼7.8K.

set the dominant frequency at 560±30T. Panel c and d display the fitting for the effective mass m^* and the Dingle temperature T_D. By the Lifshitz-Kosevich (LK)

expression, the oscillation amplitude is proportional to the thermal damping factor

$$R_T = \alpha T m^*/B \sinh(\alpha T m^*/B) \tag{3.5}$$

where $\alpha = 2\pi^2 k_B m_e/e\hbar$ and m^* the effective mass. The Dingle damping factor is

$$R_D = \exp(-\alpha T_D m^*/B) \tag{3.6}$$

where $T_D = \hbar/2\pi k_B \tau_S$ is the Dingle temperature with τ_S the scattering rate. We obtained an effective mass $m^* \sim 1.70 \pm 0.07 m_e$ and a Dingle temperature T_D=7.8K. There results are in agreement with previous studies[6, 13, 24].

3.4 Discussion: Vortex Liquid State

Answering the question whether vortex liquid state persists into an extensive region on the phase diagram is not only one of the original motivations of this project, as will be discussed below, it is also central to understanding physics in the pseudogap region and the competing orders. This section will first present arguments from torque magnetometry supporting an extensive vortex liquid state, then discuss in detail about conflicting arguments from thermal conductivity studies in Section.3.4.1.

Fig.3.13 shows the observed magnetism M_{obs} plotted against magnetic field. This result supports a very basic claim that the superconducting state persists into temperatures much higher than T_C in the form of vortex liquid: 1st a diamagnetic signal is observed, indicated by M_{obs} being negative; 2nd the observed diamagnetic signal is much larger than any alternative sources other than (fluctuating) superconducting states; 3rd this diamagnetic component is nonlinear with respect to applied magnetic field.

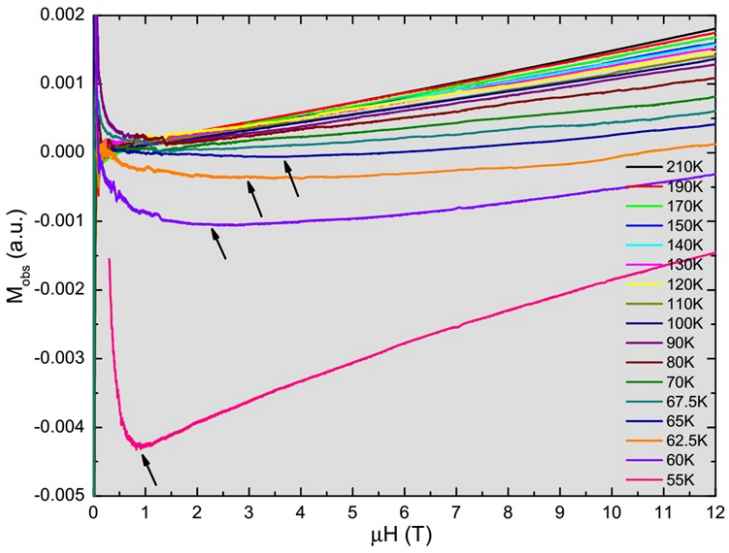

Figure 3.13: M_{obs} of $YBa_2Cu_3O_{6.55}$ through torque-magnetometry measurement.

This non-linearity would result in a local minimum in M_{obs}, position of which moves rapidly towards higher magnetic values with increasing temperature. This observation is in agreement with previous study on related cuprate systems[19] as shown in Fig.3.14, and could serve as additional proof that superconducting state in $YBa_2Cu_3O_{6.55}$ persists beyond critical temperature T_C in the form of superconducting vortex liquid.

3.4.1 Conflicting Arguments with Thermal Conductivity Measurements

In a previous study[8], a step-like feature on thermal conductivity was observed around ~20 Tesla for YBCO $p = 0.11$. Our collaborator from Princeton University also observed a similar feature as shown in Fig.3.15 panel a. Authors of [8] interpret this step-like feature as evidence of a lower estimation of H_{c2}. However, we do not agree.

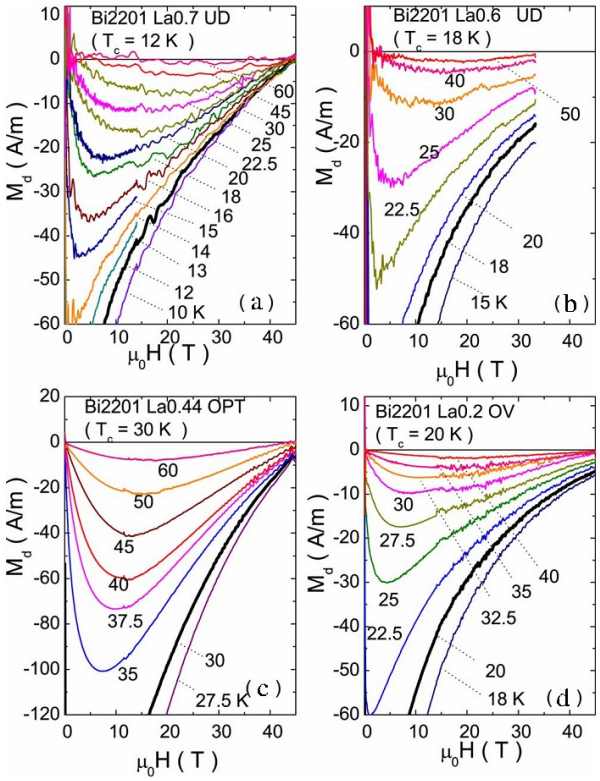

Figure 3.14: M_d of 214-system at temperatures much higher than T_C, through torque-magnetometry measurement [19].

Thermal conductivity in this system κ has two parts: the electronic part κ_e and the phonon part κ_p. For κ_p, increasing H causes increased phonon scattering by quasiparticles. But the relevance of this effects need to be compared with other contributions to κ_p. For κ_e, increasing applied magnetic field H will excite quasiparticles but also enhances vortex scattering. The two effects cancels out until H approaches H_{c2} where vortex is close to be removed. The authors of [8] argues κ_e is the main contribution to the step-like feature.

Similar to the case of a type-II superconductor at $T \ll T_c$, κ_e in the normal state above H_{c2} is limited by the elastic mean free path l_0. When applied magnetic field is below H_{c2}, vortices introduce an extra scattering mechanism. If the normal state

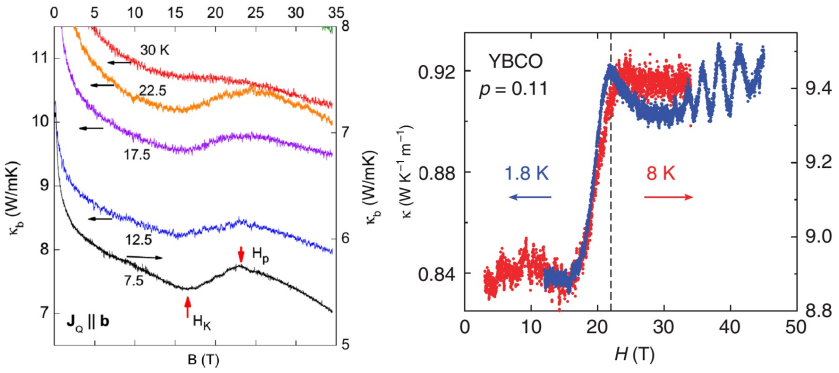

(a) (b)

Figure 3.15: Panel a: thermal conductivity results of our collaborators. Panel b: thermal conductivity results of Ref.[8]

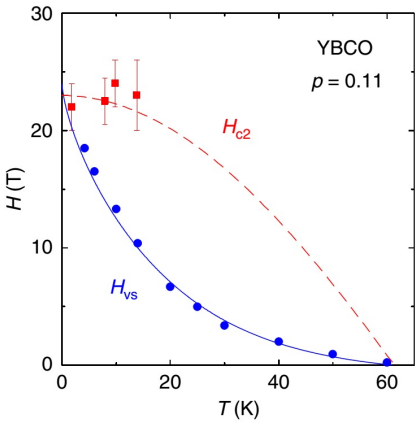

Figure 3.16: Phase diagram by Ref.[8], indicating a lower estimation of H_{c2} for $YBa_2Cu_3O_{6.55}$.

mean free path l_0 is much longer than the inter-vortex separation ξ_0[7], the mean free path will suddenly become much shorter when applied magnetic field drops below H_{c2}, creating the step-like drop in thermal conductivity[29]. Based on this argument, authors of [8] used the lower edge of the step-like drop to characterize H_{c2}, and obtained their estimation of H_{c2} dependence on magnetic field/temperature as

[7]defined as the $T = 0$ coherence length $H_{c2} = \Phi_0/2\pi\xi_0^2$.

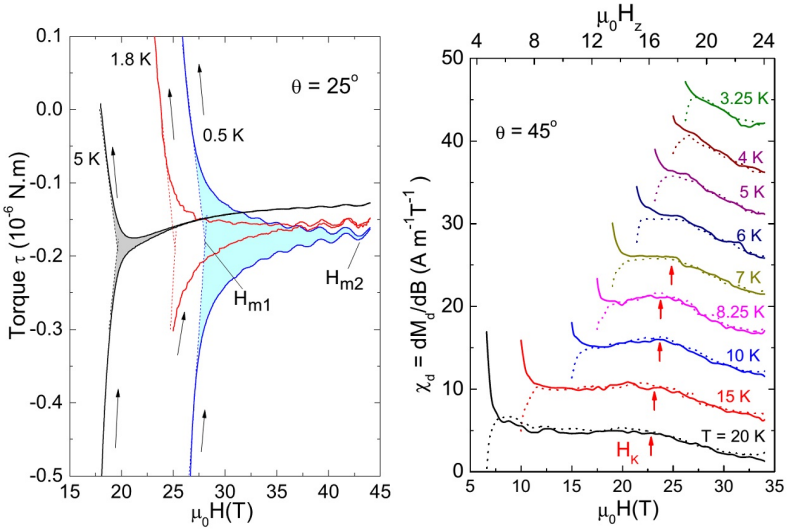

(a) (b)

Figure 3.17: Temperature dependence of the boundary between vortex solid and vortex liquid through torque-magnetometry measurement.

shown in Fig.3.16.

However, such an estimation is cavalier at best. First, in their publication, all the data for YBCO $p = 0.11$ were obtained below 10K, thus there is no real supporting evidence for the depicted temperature dependence of H_{c2} in Fig.3.16.

Second, from panel a of Fig.3.17, one could sea that the hysteresis persists upto at least 20 Tesla at 1.8K, thus the blue step-like feature in Fig.3.15 sits on the boundary of vortex solid state. However, the boundary is ∼10 Tesla at 10K by panel b of Fig.3.17, much lower than the ∼20 Tesla position of the red step-like feature of thermal conductivity at 8K. In other words, the weak temperature dependence of step-like feature of thermal conductivity does not match the strong temperature dependence of superconducting vortices.

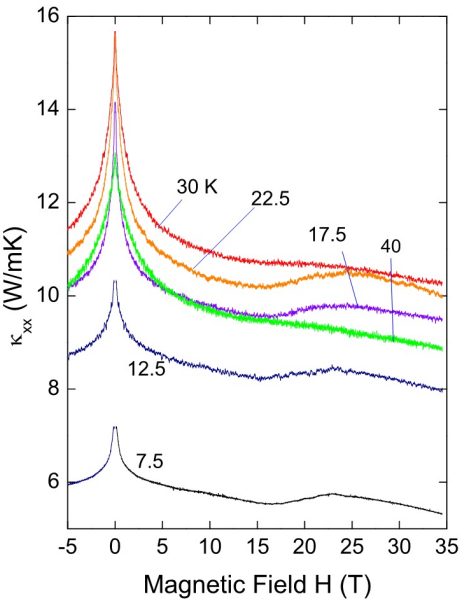

Figure 3.18: Temperature dependence of the thermal conductivity κ_{xx} of ortho-II YBCO $p = 0.11$.

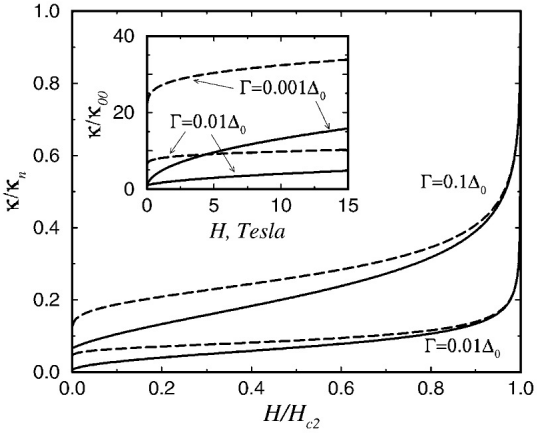

Figure 3.19: Field dependence of the thermal conductivity at T=0 for scattering in the unitarity (solid lines) and Born(dashed lines) limits. Adapted from[27].

Finally, the mechanism creating a drop on thermal conductivity only requires a reduced mean free path due to vortex scattering. With increasing temperature or magnetic field, the vortices will become unpinned from the crystal and diminished

in number, and their scattering effect on mean free path will weaken to a point where mean free path become the same as in the normal state. This does not call for a total suppression of superconducting state. As a matter of fact, the change of thermal conductivity corresponding to the step-like feature is estimated to be ∼15% of that caused by vortices at lower temperature as shown in Fig.3.18, as opposed to the ∼50% predicted by a theoretical study[27] shown in Fig.3.19.

Instead, we propose that this step-like feature on thermal conductivity is closely related to the "kink" feature observed on magnetometry. We agree with the argument that an rapid increase of thermal conductivity with increasing magnetic field at $\sim$ 18 Tesla is due to reduced vortex scattering. This is also reflected in magnetometry measurement as a rapid decreasing of diamagnetic signal as shown in Fig.3.5.

3.5 Discussion: Coexisting Orders

In the previous section, we have discussed and linked the "kink" feature from magnetization and the step-like feature from thermal conductivity. We believe that this two features from different experimental methods reflect the same physics process, based on two arguments: 1st, both features show up in the same region on the temperature-magnetic field phase diagram for doping $p = 0.11$; 2nd, the processes indicated by both observations are in agreement with each other. The latter argument is also the stronger one of the two.

We conclude that, the "kink" feature and the step-like feature are the result of a same transition, happening from 15 to 20 Tesla, at temperatures downward from 40K to at least 5K. We believe that this transition is competition between superconducting state and the charge density state in nature, with charge density state becoming the dominant state above this transitional region. However, given

the evidence from Fig.3.13 indicating that vortex liquid persists into much higher temperature, we propose that the competition between superconducting state and the charge density state is only relative - the two states competes and coexists in a large overlapping region on the phase diagram.

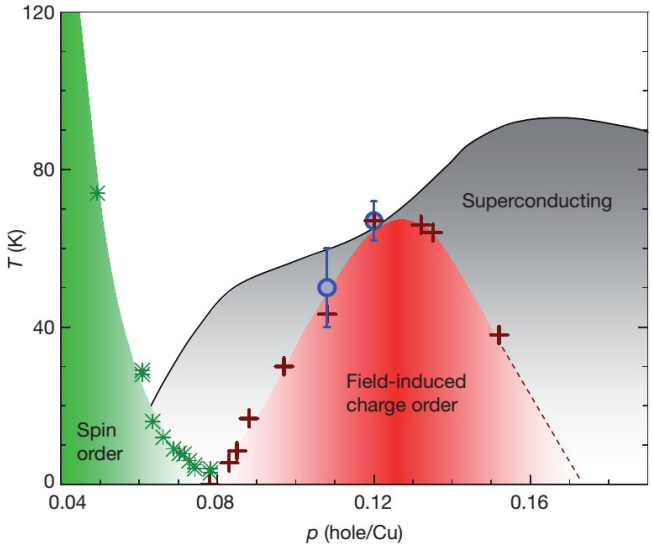

Figure 3.20: Phase diagram from Ref.[32] through nuclear magnetic resonance measurement.

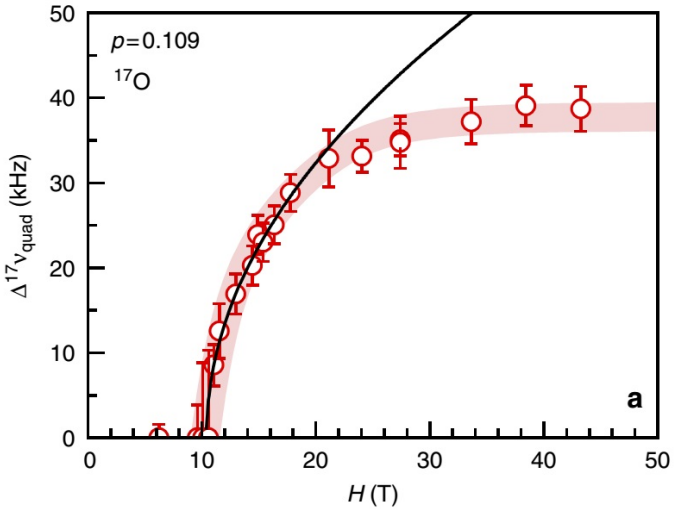

Figure 3.21: Nuclear magnetic resonance result from Ref.[33] for doping p=0.11.

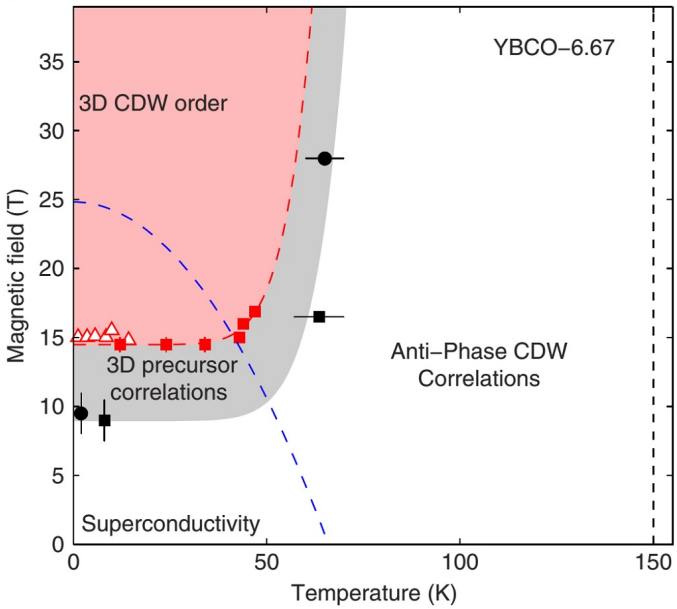

Figure 3.22: Phase diagram from Ref.[5] through hard X-ray scattering.

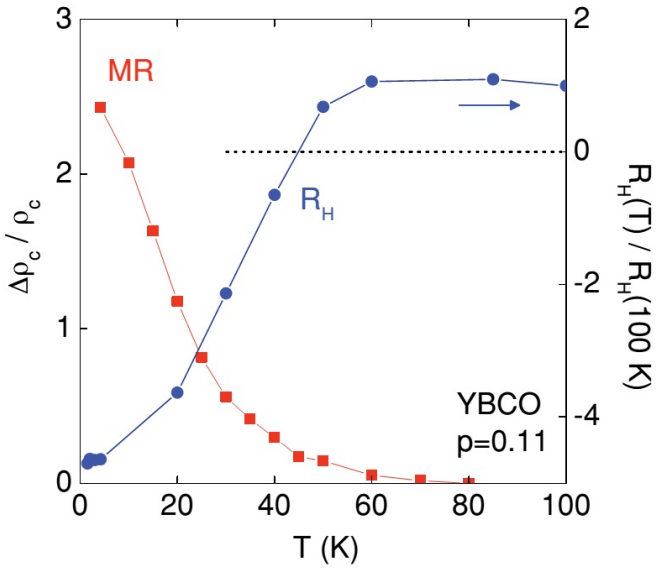

Figure 3.23: The in-plane Hall coefficient R_H from Ref.[15].

In the study of pseudogap and its various orders, results from various experimental methods need to be combined to obtain a more complete picture of the physics process. Although our interpretation of the "competing orders" as well as our es-

timation of upper critical field H_{C2} are different from many studies, yet the line drawn by H_k on our phase diagram Fig.3.8 is consistent with various experimental methods, particularly those methods that are sensitive to charge order in one hand and insensitive to superconducting order in the other hand.

The first to compare is the NMR result in Fig.3.20 from Ref.[32], where the onset temperature of field-induced charge order is fixed at 40 K for doping level p=0.11. It is very revealing that this is also the onset temperature of the "kink" feature. Furthermore, a more recent NMR result in Ref.[33] revealed a deviation of the quadrupole part of the splitting of the O(2) line from the square-root fitting happens at 20 Tesla, roughly matching the magnetic field range of "kink" feature/step-like feature.

The second to compare is the hard X-ray result from Ref.[5] shown in Fig.3.22. Their X-ray results combined with thermal Hall coefficient [9] indicates a temperature insensitive boundary of three-dimensional charge density wave order with an onset temperature very similar to ours.

Finally, the in-plane Hall coefficient R_H from Fig.3.23 indicates a transition from hole-dominance to electron-dominance. Again, such transition overlaps the region outlined in our phase diagram Fig.3.8 through torque-magnetometry method and thermal conductivity method.

3.6 Potential Future Study

Our study was limited to a single doping level p=0.11. However, the deviation of the quadrupole part of the splitting of the O(2) line from the square-root fitting does demonstrate a strong dependence on doping, as shown in Fig.3.24. If future study using torque-magnetometry and thermal conductivity could reveal a

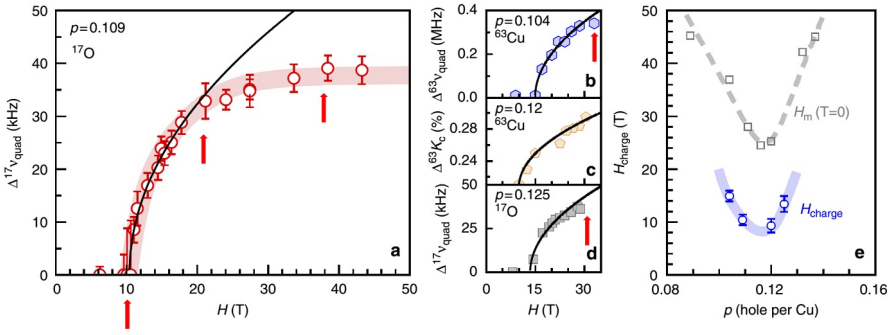

Figure 3.24: Nuclear magnetic resonance result from Ref.[33] for doping p=0.104∼0.125.

strong doping level dependence, with the transitional region moving rapidly towards higher magnetic field, then it would be a stronger evidence that our results as well as results from Ref.[33][15][5] are measuring the same competing process between superconducting state and the charge density wave state.

Chapter 4

Torque-Magnetometry in Pulsed Magnetic Field

Considering the discussions offered by Chapter.3, it is very helpful if one could have access to magnetic field stronger than 45 Tesla. Furthermore, given the diverging temperature dependence of H_{irr}, higher magnetic field is required to answer the question regarding boundary of vortex liquid state in extremely low temperature.

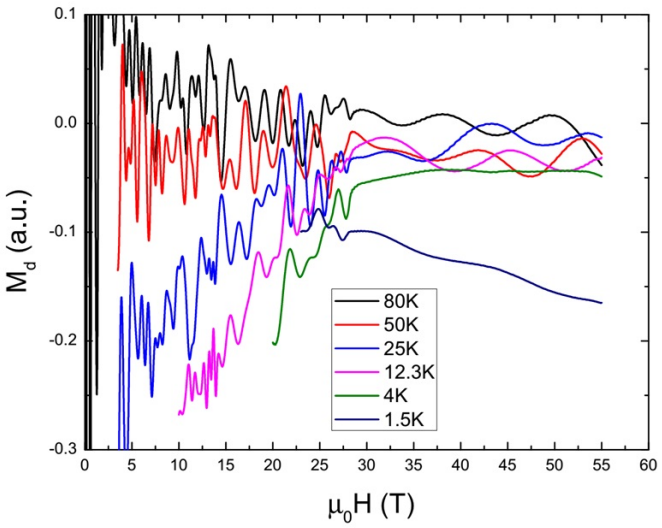

Figure 4.1: Magnetometry results in 60 T long-pulse system from Summer 2013.

To achieve higher magnetic field than 45 Tesla, currently available technology calls for pulsed magnet system. Given the mechanical nature of the magnetometry method, pulsed magnetic field environments create many challenges, to the extend that the magnetometry method needs to be reinvented.

Nonetheless, it is important to note that, our previous study of underdoped YBCO in DC magnetic field environment was also partially inspired by our pre-

liminary results in pulsed field experiments, as shown in Fig.4.1. This summer 2013 data, which was (incorrectly) interpreted as evidence of abnormal behavior in magnetization, was one of the driving factors of our DC field study that started in winter 2013.

4.1 the Facility and Experimental Condition

4.1.1 the Magnet System

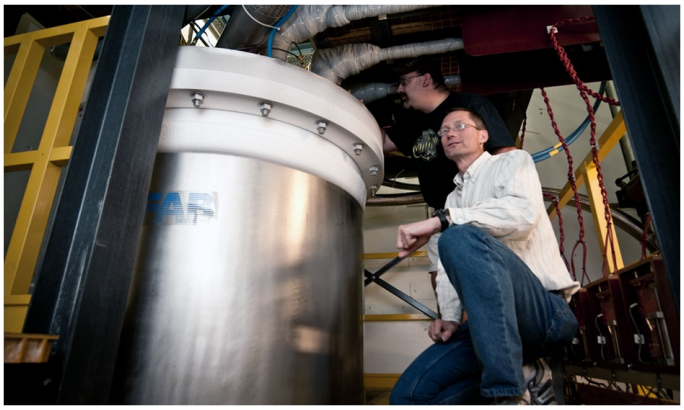

Figure 4.2: The 65 Tesla long pulse magnet. Picture from NHMFL.

Figure 4.3: Power source for the 65 Tesla long pulse magnet. Picture from NHMFL.

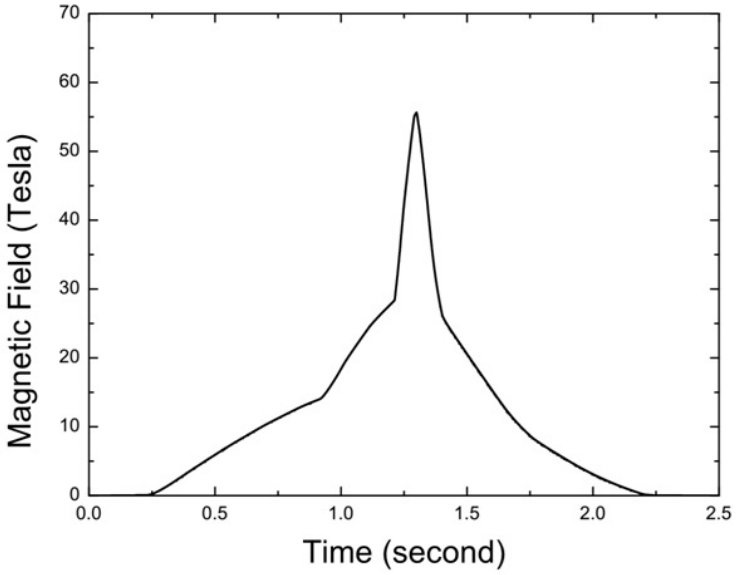

Figure 4.4: Magnetic field vs time profile of 60 Tesla long pulse. The 65 Tesla long pulse magnet is capable of several different profiles.

Figure 4.5: The 65 Tesla short pulse magnet's coil (lower left). Picture from NHMFL.

The 65 Tesla long pulse magnet system is a huge resistive magnet driven by an inertial energy restoration-release system, as shown in Fig.4.2 and Fig.4.3. The magnet system has a semi-controllable pulse profile with a duration ∼2 seconds.

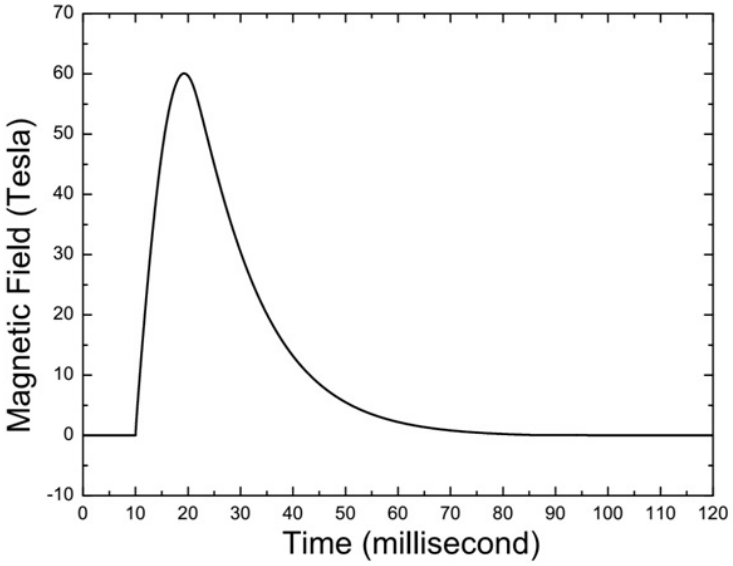

Figure 4.6: Magnetic field vs time profile of 60 Tesla short pulse.

Comparatively, the 65 Tesla short pulse magnet system is a smaller setup (coil shown in Fig.4.5) driven by capacitor bank with a duration of less than 100 milliseconds.

The first difference between these two systems is their pulse profiles. The pulse profile for the long pulse system is mostly symmetric while that for the short pulse system is not. This is because the discharging process of the inertia system was designed with certain level of control while that of the capacitor bank was not. The symmetric profile of long pulse system is very helpful for experiments that need to compare up-sweep and down-sweep data. However, even for the long pulse, the most valuable part of the pulse - when magnetic field is stronger than 45 Tesla - would linger for only $\sim$0.2 second with sweeping speed 300 Tesla/second. For the short pulse, the high field parts is even shorter with sweeping speed $\sim$3000 Tesla/second.

The high sweeping speeds of the pulse system creates challenges in experimental setups' responsiveness. For example, the turning point of magnetization in Fig.4.1

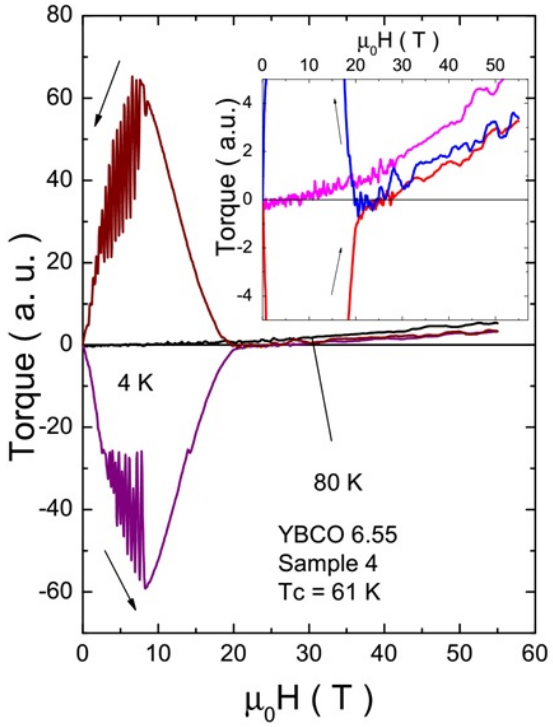

Figure 4.7: 55 Tesla long pulse shot of YBCO 6.55.

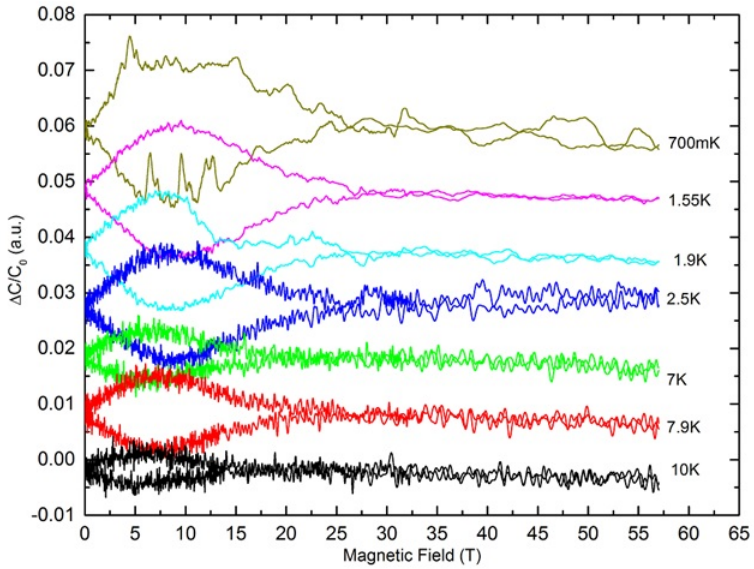

Figure 4.8: 55 Tesla long pulse shots of YBCO 6.55 in summer 2013.

at ∼30 Tesla is most likely due to cantilever not responding fast enough to the change of sweeping speed as shown in Fig.4.4. Later improvements on our design of cantilevers has made the situation in long pulse quite similar to that of DC field, as shown in Fig.4.7. But we are still facing responsiveness problems in short pulse experiments.

The second difference between these the long and short pulse system is their noise levels and sources. The dominant noise source is a constant mechanical vibration due to the three-phase method of injecting electric power into the magnet coil. This mechanical noise can be seen from Fig.4.8. It has a characteristic frequency of ∼300 Hz, persists through the entire pulse and is at least one order of magnitude larger than the electric noise. On the other hand, the short pulse system has a very different noise source which will be discussed in detail below.

4.1.2 the Fridge and the Probe

The principle of low temperature fridge and probe design is subject to two unique considerations: 1st, the bore size of the magnet is very small; 2nd, the extremely large dB/dt environment. The former means the sample sapce of the low temperature fridge has to be designed with the shape of a thin, long tail while the latter means the fridge and probe system needs to be made with nonmetallic material. The rotator probe that is used to generate the best short pulse data are shown in Fig.4.9. As can be seen, the sample space is very narrow, just 4 mm. Fig.4.10 shows a typical cantilever used for pulsed field experiment.

Furthermore, due to the limited magnet bore size, the thermal link and isolation of the low temperature fridge is also "spartan" compared with traditional fridge designs. The probe, as in Fig.4.9, once loaded with sample and device, is inserted into a probe shielding. The shielding is also of a long, tin tail shape. The diameter

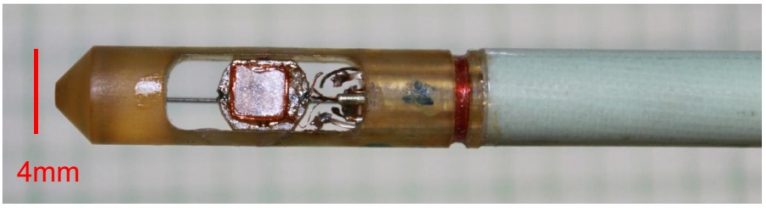

Figure 4.9: Rotator probe.

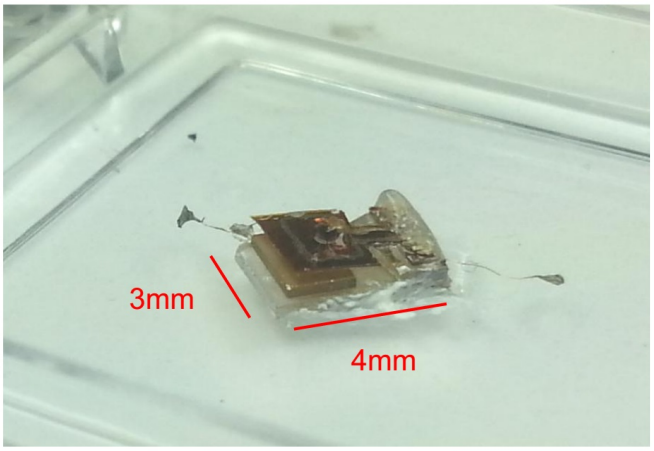

Figure 4.10: A typical cantilever used for pulsed field experiment.

of the tail usually 1 or 2 mm larger than that of the probe. The probe and its shielding is then inserted into the fridge. Thus, the lower part of the fridge-probe system has two separated spaces: the sample space inside the probe shielding and the fridge space outside probe shielding. There is no thermal isolation between the two.

The fridge-probe system has three modes of operations in terms of temperature and the condition of sample space: 1st, gaseous ^{4}He environment in sample space for temperature down to 1.4 K; 2nd, liquid ^{4}He environment in sample space for environment between 4 K and 1.4K; liquid ^{3}He environment in sample space for temperature down to 300 mK. For all these operational modes, the fridge is space filled with liquid ^{4}He and pumped, providing the cooling power.

Please note that there is a key difference compared with conventional fridge design in that there is no thermal isolation between the sample space and the fridge space. This was proven to cause difficulties in fine temperature control, particularly for the liquid ^{4}He mode.

4.1.3 the Cantilever Design

Compared with DC field experiments, the cantilever design for pulse field experiments has a lot more considerations. First, due to the extremely large dB/dt and the size limitations, cantilevers are made of kapton with button surface coated with Aluminum. The size of the cantilever is limited to no more than 3 by 4 mm.

Second, one needs to consider the triad of dynamical range, sensitivity and susceptibility to noise. The main control variable here is the thickness of the cantilever. In earlier experiments, we tried 5 mil thickness in order to achieve a larger spring constant. This is in part due to previously successful pulse field magnetometry experiment (by other groups) using piezo-cantilever. The rational and choices for a correct cantilever design will be discussed in detail in the following sections.

4.1.4 DAQ system

The DAQ system in the NHMFL, LANL branch is mainly based on high speed digitizer. This architect is surprisingly simple and powerful. However, for all of the experiments that will be discussed in this chapter, the actual DAQ system is no different from that of DC field experiment, in the sense that we used analog capacitance bridge and digital lock-in. The only minor difference is that we drove the analog capacitance bridge to its upper frequency limit and that we used the digitizer to acquire data from lock-in through analog outputs instead of GPIB like the situation in DC field.

It is worth mentioning that, although we designed and made digital capacitance bridge chips and intended to deploy it in the sample space, exploiting its high frequency capability, the digital capacitance bridge chip was never fitted onto the probe due to insufficient sample space.

4.2 the 60 Tesla Short Pulse Experiment

This section will discuss the experimental method for 60T short pulse experiment; or more precisely, capacitance-cantilever method for magnetization measurement under conditions where the magnetic field changing rate is in excess of 6000 Tesla per second.

There will be a chronicle of data that we collected during 3 experimental trips, failed or successful, from 2013 to 2015. Through this chronicle one will see how we singled out damping from environment as the single most important control variable as well as how we figured out an inherent time delay, which is on the part of fridge and probe, will actually save the experiment from violent mechanical noises.

In addition to experiments and data analysis, computational simulation proved to be an essential tool for understanding, analyzing and designing pulsed magnetic field experiments. Through out this section, we will go through results from extensive computational simulations, both proving/disproving our assumptions/conclusions drawn from data as well as offering new insights into the experiment.

This section is organized as the following: subsection 4.2.1 will discuss why damping of the cantilever from the sample space environment is the most important control variable; subsection 4.2.2 will discuss noises encountered during experiments as well as methods of controlling them; subsection 4.2.3 will discuss the signal retrieval technique, which is essential for analyzing data.

4.2.1 the Damping Factor and Characteristic Frequency of Cantilever

In DC field, the behavior of cantilever is static, described by Hooke's law $F = -kx$, according to which cantilever's response is linear with sample's response to magnetic field $H * M$.

In pulsed field, however, the behavior of cantilever is one of dynamic representation of sample's response to magnetic field. While in the DC magnetic field the cantilever has several minutes to adjust to sample's changing behavior from 11 Tesla to 45 Tesla, in the pulsed magnetic field the cantilever only got 8 s from 0 Tesla to 60 Tesla. Thus the best starting point of analyzing pulsed magnetic field experiment would be Equation.4.1, where F_{ext} would include sample's response to magnetic field as well as all kinds of noise exerted upon the cantilever.

$$\frac{d^2x}{dt^2} + 2\zeta\omega_0\frac{dx}{dt} + \omega_0^2 x = F_{ext} \tag{4.1}$$

the Ringing Cantilever and the Characteristic Frequency

Here we use as examples our data on $BaFe_2(As_{0.51}P_{0.49})_2$.From Figure.4.11 one could clearly observe that during these 60T short pulse shots, the cantilever is ringing violently, thus how much the signal represents sample's response to magnetic field is questionable. For $BaFe_2(As_{0.51}P_{0.49})_2$, its T_c is around 10 K, which is why one could only observe hysteresis on the down sweep of 10 K shot. Please note that the huge bump around 15 millisecond is not the up sweep hysteresis, rather it might be the signal of sample's paramagnetic component since a 20 T melting point (judging from 10 K down sweep) would be reached within ~2 millisecond in the up sweep. Or even worse, the huge bump might just be the cantilever over shooting due to sample's response to the initial skin-effect magnetic field kick (please see Section 4.1.1), since the peak of the bump arrives before the peak of magnetic field.

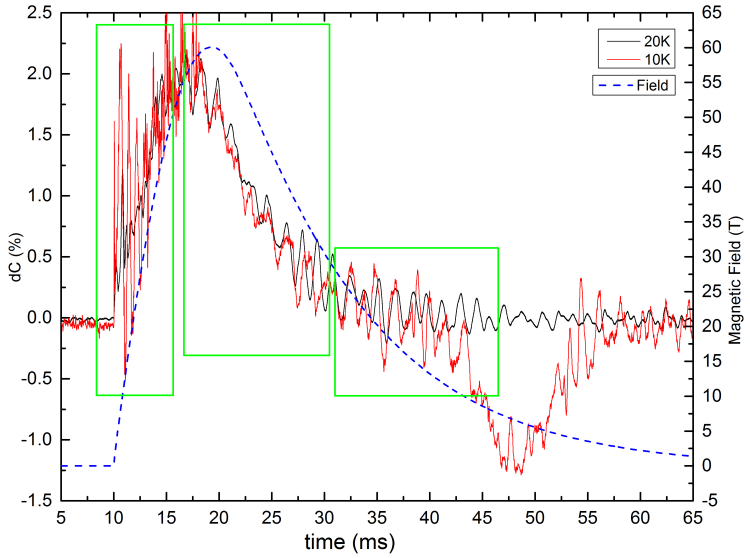

Figure 4.11: 60T short pulse, dC(percentage) vs time of $BaFe_2(As_{0.51}P_{0.49})_2$ at 20 K and 10 K, in ^{4}He gas, with 3-mil kapton cantilever and straight probe. Please note that according to arguments at Section.**??**, our signal is dominated by mechanical noise rather than electrical noise.

Further more, Figure.4.11 reveals that the cantilever is oscillating in different patterns. Within the first green window, the cantilever is ringing at ∼1.2 kHz with very good sinusoidal shape. With the third green window, the cantilever is at ∼700 Hz with slightly worse sinusoidal shape, while within the second green window, the cantilever shows a mixture of more than one frequencies. We believe that this ∼1.2 kHz frequency is the characteristic frequency of the 3-mil kapton cantilever. As for the second lower ∼700 Hz frequency, it turned out to be a mechanical noise due to the combination of the magnet, the fridge and the straight probe. Also, please note that while the characteristic frequency of a cantilever is relatively stable, the frequency of the mechanical noise is less stable and varies with different magnet, fridge as well as different conditions of the probe. Both claims will be substantiated in more detail during the following sections.

the He_4 Liquid and Damping

The most important point of understanding pulsed magnetic field experiment of capacitance cantilever method is that the cantilever is performing a forced oscillation with certain damping level. The most desirable external perturbing force would, of course, be sample's response to magnetic field. The damping, however, is a much less straight forward story. It turns out that damping is a double edged sword for capacitance cantilever method, both making it feasible as well as rendering it inherently unsuitable for measuring dHvA effect, which is usually the most important objective. Here we will only discuss how damping makes the capacitance cantilever method feasible; in the discussion section of this chapter we will talk about its inherent weakness.

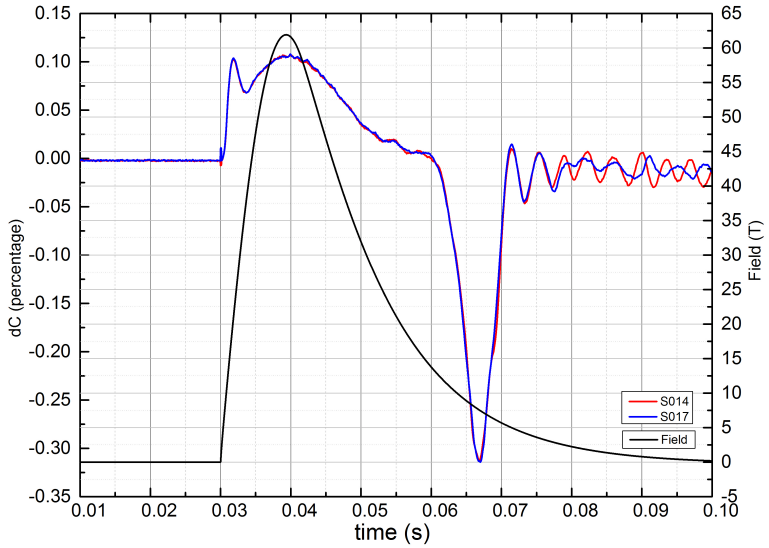

Figure 4.12: 60T short pulse, dC(percentage) vs time of $BaFe_2(As_{0.51}P_{0.49})_2$ at 1.5 K, in ^{4}He liquid, with 1mil kapton cantilever and Fedro's rotator probe.

Figure.4.12 is two 60T short pulse shots of $BaFe_2(As_{0.51}P_{0.49})_2$ at 1.5 K, almost the same condition of the shots in Figure.4.11, except that the shots in Figure.4.12

are in liquid ^{4}He. The difference between these shots is dramatic: in Figure.4.12, there is no ringing observe during most of the pulse, and the overall percentage signal is much smaller. The reason, we believe, is that in liquid ^{4}He, the cantilever is at least close to critical damping while it is under damped in gaseous ^{4}He. Thus, one could use shots in gaseous environment to pin point characteristic frequencies of cantilever, which is exactly how we obtained data in Figure.4.13. From this figure, one could observe a ∼700 Hz frequency through out most of the pulse. We believe that this is the characteristic frequency of the 1-mil kapton cantilever since in a gaseous environment the cantilever would be under-damped and displaying its f_c. Also, please note that this ∼700 Hz frequency is in match with the ∼1.2 kHz frequency of 3-mil kapton cantilever, as thinner cantilever should have a lower characteristic frequency.

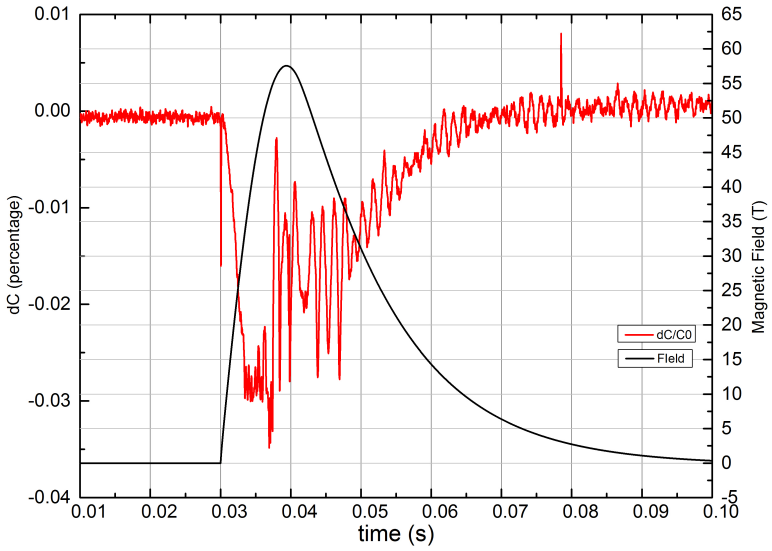

Figure 4.13: 60T short pulse, dC(percentage) vs time of $[(Li_{1-x}Fe_x)OH](Fe_{1-y}Li_y)Se$ at 6 K, in ^{4}He gas, with 1mil kapton cantilever and straight probe.

Armed with these conclusion, we could look at Figure.4.14, where several shots of $[(Li_{1-x}Fe_x)OH](Fe_{1-y}Li_y)Se$ were taken at ∼2 K in liquid ^{4}He. First, one could

notice that there are ∼7 periods of reproducible oscillating signal during the first 20 milliseconds of the downsweep. However, this is not due to quantum oscillation of the sample because during our experiments at 45 Tesla DC facility at NHMFL, we could not observe any dHvA signal from the same sample upto 45T. Thus it is inconceivable how one could observe such a strong quantum oscillation pattern starting from ∼10 Tesla. Second, one could notice that the ringing here has a lower frequency of ∼300 Hz, which is roughly equal to the oscillating frequencies towards the very end of pulse in Figure.4.12. Since in both data sets the cantilever is at least critically damped by ^{4}He liquid, we believe this ∼300 Hz frequency is the characteristic frequency of the mechanic noise due to the magnet, fridge and probe[1]. Third, we believe that, although the cantilever is at least critically damped by ^{4}He liquid, the probe remains under-damped (with a damping factor at most 0.5). Fourth, accepting the assumption that the probe is under-damped and the fact that there are ∼7 periods of reproducible oscillating signal during the first 20 milliseconds of the down sweep, one could conclude that there is a mechanical "kick" on the probe at around 10 milliseconds into the pulse. We will discuss the time-delayed mechanical noise in more detail in Section 4.2.2.

Further more, one might notice that in Figure.4.13 and Figure.4.14, there are strong oscillating patterns of higher frequencies within the first 10 milliseconds of the pulse. Interestingly, analysis of Bdot data[2] reveals a corresponding feature, as shown in Figure.4.15, which might offer more insights into pulsed magnetic field experiments. As demonstrated in Figure.4.15, different probes have vastly different characteristics; in the following section one will see that the quality of probe is the second most important factor in performing successful pulsed magnetic field experiments.

[1]Please note that the f_c of mechanic noise depends on the combination of magnet, fridge and probe. Data sets of Figure.4.11 and Figure.4.14 were obtained on different magnets.

[2]More introduction about Bdot measurement could be found in Section 4.1.1.

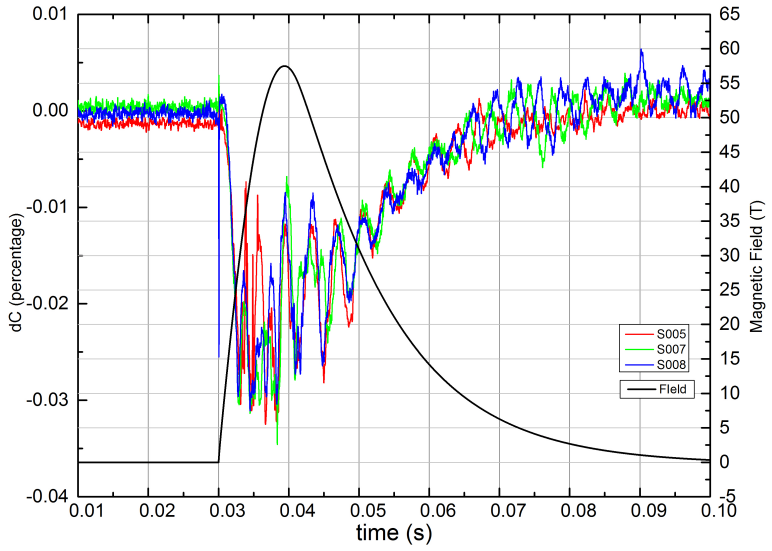

Figure 4.14: 60T short pulse, dC(percentage) vs time of $[(Li_{1-x}Fe_x)OH](Fe_{1-y}Li_y)Se$ in ^{4}He liquid, with 1-mil kapton cantilever and straight probe. Shot 5 at 2.4 K while shot 7 and 8 at 1.4 K.

For both Fedro's and John's rotator probe, one could observe a harmonic oscillating pattern of ∼4.8 kHz at ∼2.5 millisecond into the pulse. Although it is not shown here, for both probe, this oscillating pattern is so persistent, that not only its frequency but also its phase are stable (within each probe). To observe such a pattern, there are only two possible explanations: first, the probe is oscillating, thus Bdot coils experiences varying magnetic field (more precisely, oscillating speed at which the magnetic field is increasing); second, this is due to the magnet itself oscillating, or the way the current passing through the magnet (in other words, this is not due to the probe oscillating). Since a very stable frequency is observed from two different probes, as well as the fact that this pattern only lasts about 2.5 millisecond during which the magnetic field is increasing at its highest rate, we have to believe this is due to the latter reason. Besides, we already know that the characteristic frequency of the probes are much lower. As for why the oscillating

patterns are of different magnitudes, possible explanation would be that the Bdot coils have different coupling strength.

As for the straight probe, one could still observe this ∼4.8 kHz oscillating pattern, though it is followed by a much stronger noise. The origin of this difference would be the topic of Section 4.2.2. However, here we would like to point out that, although all d(Bdot)/dt curves extends smoothly past the 60 millisecond mark, it does not indicate that the probes are quiet, or not doing mechanical oscillations. The truth is rather the opposite. The reason that one could not observe these mechanical oscillations is because once past the 60 millisecond mark, the magnetic field is decreasing at a much slower rate and the Bdot coil, which response to d(B)/dt, would naturally no longer be able to pick up any signal any more.

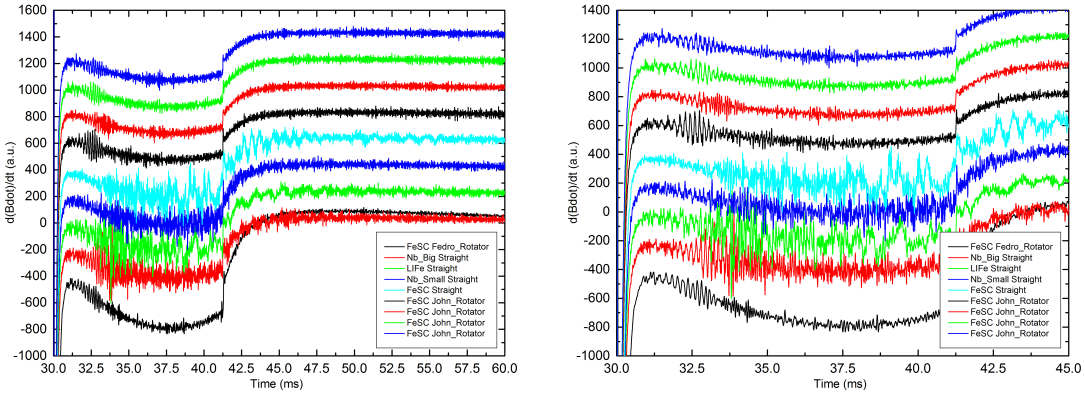

Figure 4.15: d(Bdot)/dt vs time with various probes and Cell-1 magnet. Data taken during Aug 2015 trip.

Before concluding this section, we want to point out that, although we are confident that the cantilever is at least critically damped, we could not have an estimation of the damping factor directly from the data. As a matter of fact, so long as the damping factor is larger than 0.5 (which is still under-damped), the cantilever wouldn't demonstrate free oscillating behavior. Section 4.2.1 will offer a computa-

tional solution to this question. Further more, we offer a table summarizing all the frequencies we observe directly from our data.

Table 4.1: Frequencies observed directly from 60 Tesla Short Pulse Data.

Frequency	Data Source	Classification
~1.2 kHz	Dec2014, $BaFe_2(As_{0.51}P_{0.49})_2$	F_c of 3-mil kapton cantilever
~700 Hz	Aug2015, $[(Li_{1-x}Fe_x)OH](Fe_{1-y}Li_y)Se$	F_c of 1-mil kapton cantilever
~300 Hz	Aug2015, $[(Li_{1-x}Fe_x)OH](Fe_{1-y}Li_y)Se$	F_c of straight probe and Cell-1 magnet
~700 Hz	Dec2014, $BaFe_2(As_{0.51}P_{0.49})_2$	F_c of straight probe and Cell-3 magnet
~4.8 kHz	Aug2015, Cell-1 magnet	F_c of Cell-1 magnet, fridge and potentially the probe

Computational Simulation: Interpaly of Characteristic Frequency and Damping Factor

One interesting observation from Figure.4.12 is that the magnitudes of up and down sweep hysteresis are very different. Actually, the ratio is consistently ~3.1. This is clearly a distortion due to the slow response of capacitance cantilever method in pulsed magnetic field, as results from DC magnetic field measurements as well as alternative methods in AC magnetic field [25] indicating the magnitudes of hysteresis should be almost equal. Even during our 60 Tesla long pulse experiments on the same sample, see Figure.4.16, magnitudes of the hysteresis are symmetric.

There are a few potential explanations for this phenomenon:

First, the cantilever's F_c is too low that it could not catch up with fast changing signal during up sweep (up sweep hysteresis) but could catch up with the down sweep hysteresis which is much slower.

Second, the cantilever is over damped and its response to the sample has a time delay compared with sample's response to the magnetic field. And this

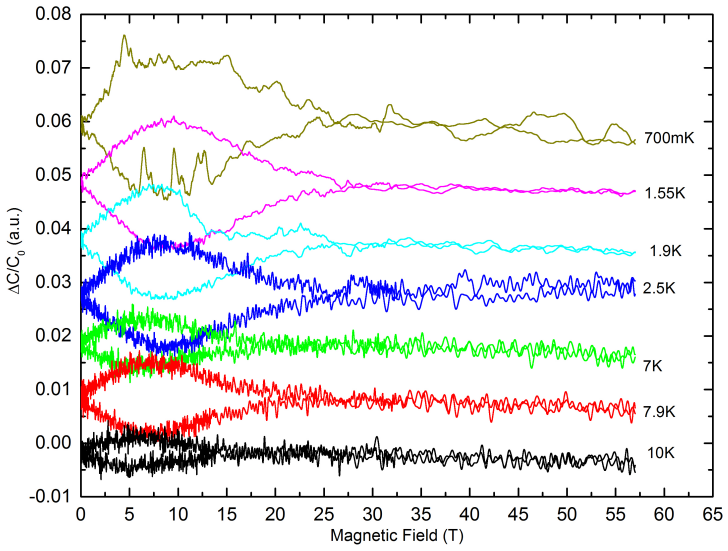

Figure 4.16: 60 Tesla long pulse, dC (percentage) vs time of $BaFe_2(As_{0.51}P_{0.49})_2$, with 5-mil kapton cantilever and straight probe.

time delay might prevent the cantilever from reaching the correct amplitude and is naturally more dramatic during the faster up sweep.

Third, the cantilever is in the nonlinear region. However, this is much less likely the case since 30% overall change is still roughly within the linear region, according to our previous experiences.

Thus, it is the interplay of cantilever's F_c and cantilever's damping factor that determines the non-symmetric magnitudes of hysteresis, from which one might be able to pin-point the damping factor. The way forward, of course, is computational simulation of the 60 Tesla short pulse experiment. Since right now we do not consider the influence of mechanic noise upon the cantilever, the equations for simulation would look like:

$$acce_{cantilever} = -A * pos - B * vel + C * F_{ext} \tag{4.2}$$

where

$$A = \omega_0^2$$
$$B = 2\zeta\omega_0$$
$$C = \text{sensitivity of cantilever to external force}$$
$$F_{ext} = \text{sample's response to magnetic field}$$

Figure.4.17 is the result of our simulation, which demonstrates that: first, as expected, the down sweep hysteresis is much less sensitive to changing parameters; second, comparing the red trace (F_c ~200 Hz, at critical damping) with the green one (F_c ~700 Hz, at critical damping), the one with lower F_c has a smaller magnitude for the up sweep hysteresis and a overall larger time delay; third, comparing the three traces sharing F_c ~700 Hz, a damping factor of at least 1.75 would result in a up/down sweep magnitude ratio of ~2; fourth, the up sweep hysteresis' magnitude drops much slower once the damping factor is larger than 1.75. Armed with these observations, as well as the fact that $BaFe_2(As_{0.51}P_{0.49})_2$ data in Figure.4.12 has several reproducible, fine features[3], it would be a save assumption that $\zeta \sim 1.75$.

Another interesting question one could raise is: what is the damping factor for the probe? From previous sections we have learned that the probe is under damped, with as the proof the ringing patterns in Figure.4.14. We could try to reproduce the former, using a pure para-magnetic signal as seed, with a sharp ~5 kHz mechanical excitation on the probe at around 2.5 millisecond into the pulse plus some weak random noise level. The equations for simulation would now look like:

[3]at beginning of the pulse, peak field and down sweep before hysteresis.

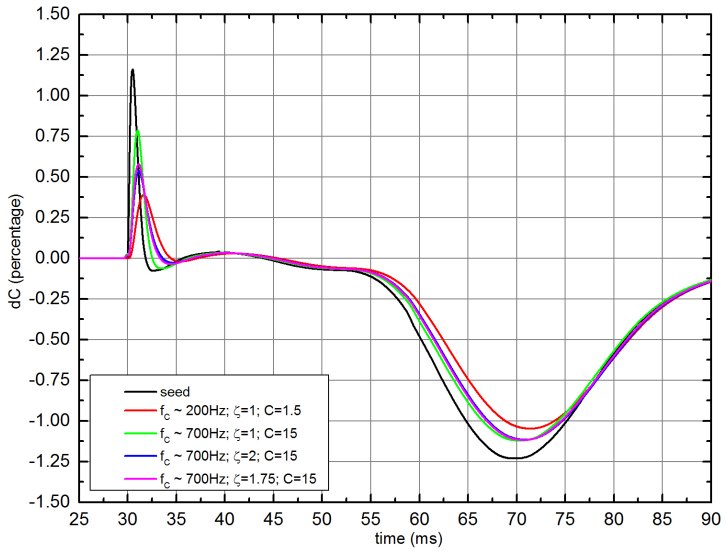

Figure 4.17: Simulation of 60 Tesla short pulse experiment, using DC field YBCO data as seed. Please note that time unit of simulation is millisecond.

$$\begin{aligned} acce_{cantilever} &= -A * pos - B * vel + C * (F_{sample} + K * acce_{probe}) \\ acce_{probe} &= -A_p * pos - B_p * vel + C_p * F_{ext} \end{aligned} \tag{4.3}$$

where

$A = \omega_0^2$

$B = 2\zeta\omega_0$

$C =$ sensitivity of cantilever to external force

$K =$ sensitivity of cantilever to vibrating probe, scaled against sample's signal

$F_{sample} =$ sample's response to magnetic field

$F_{ext} =$ external mechanical noise upon the probe

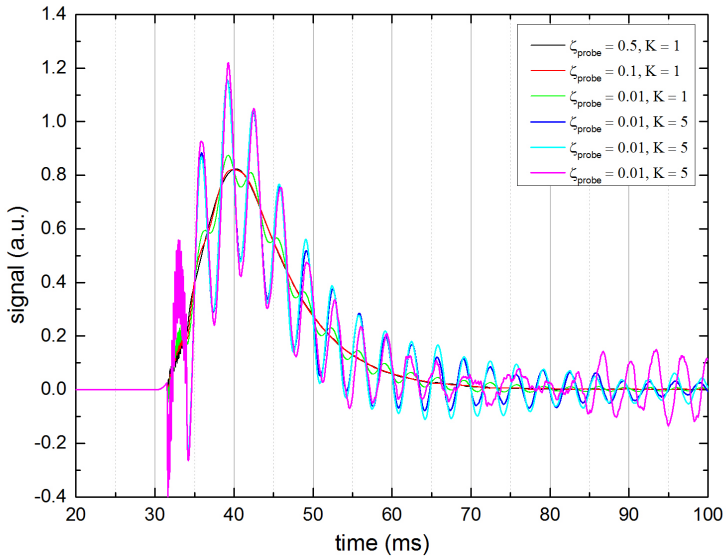

Figure 4.18: Simulation of 60 Tesla short pulse experiment, using pure paramagnetic signal as seed. The blue and cyan traces share the same parameters; the magenta trace shares the same parameters with the blue and cyan, except that its random noise level is increased to 50% of that of the ∼5 kHz excitation. Please note that time unit of simulation is millisecond.

Figure.4.18 is the result of simulation. From the first four traces, one could conclude that ζ_{probe} is at most 0.01 while the cantilever is much more (∼5 times) sensitive to probe's vibration. The last three traces are very interesting. As we increase the level of random noise from 10% to 50% of that of the ∼5 kHz excitation, both the phase and amplitude of the oscillating patterns become non-harmonic past the 60 millisecond mark. This is exactly what we observed from Figure.4.14. Thus this could be a rough indicator of how much random noise the probe received during experiment. Before concluding this section, we offer the table below summarizing all the parameters we have learned about the cantilever, probe, fridge and magnet from both data and simulation.

Table 4.2: Parameters of 60 Tesla Short Pulse Experiment.

Parameter	Data	Notes
$\omega_{cantilever}$	~700Hz	f_c of 1mil kapton cantilever
$\zeta_{cantilever}$	~1.75	over damped in He_4 liquid
ω_{probe}	~300Hz	f_c of straight probe and Cell-1 magnet
ζ_{probe}	at most 0.01	probe is only slightly damped, even with He_4 liquid in experiment chamber
K	~5	sensitivity of cantilever to probe vibration, compared against sample signal
Random Noise Level	~50%	compared against magnitude of "kick" from fridge

4.2.2 the Mechanical Noise, its Origin and Differences among Probes

Origin of Noise

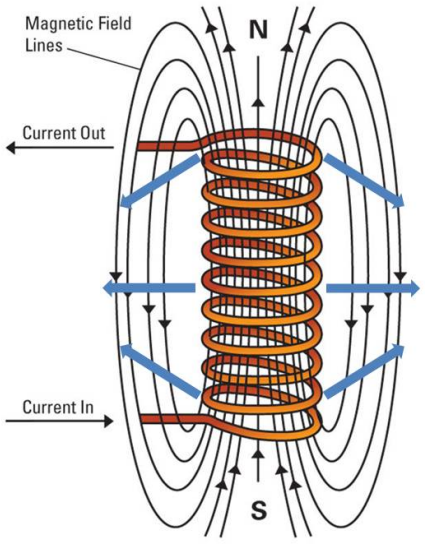

Figure 4.19: Lorentz force experienced by magnetic coil.

What is the origin of the mechanical noise? The most likely source is the Lorentz force experienced by the magnetic coil. As shown in Figure.4.19, the Lorentz force will squeeze both ends along its axis and expand radially in the middle. At peak

field, a huge amount of stress is loaded onto the coil. This stress is so big that it sometimes will cause the magnet to explode.

In a DC magnet, the magnetic field in changing in a stable, slow fashion (usually less than 0.1 Tesla per second), such that the structure of magnet has enough time to adapt to the gradually changing stress. In a AC magnet, however, the entire pulse is gone within a few dozen milliseconds. This sudden change in load will cause the magnet coil to vibrate, which we believe is the source of mechanic noise in pulsed magnetic field experiment[4]. Figure.4.20 provides a strong support for our claim, as there is clearly a excitation happened at ~90 millisecond when the pulse reached its end.

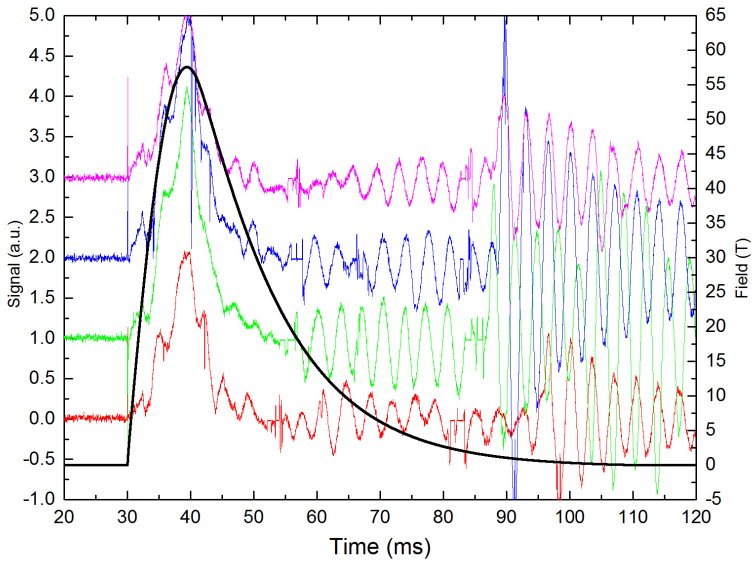

Figure 4.20: 60 Tesla short pulse, dC(a.u.) vs time of SmB_6 in ^{4}He liquid, with 1-mil kapton cantilever and straight probe.

[4]Please note that, magnet coil vibration will be induced not only by rapid loading/unloading of stress, but also by rapid change in the speed at which stress is loaded/unloaded.

Differences among Probes

One might have noticed the dramatic differences between Figure.4.12 and Figure.4.14. As argued in previous sections, in both figures, the oscillating patterns are due to an under-damped probe vibrating at its characteristic frequency. And such vibration could only be attributed to mechanical noise originating from the magnet and transmitting through the fridge onto the probe. However, the onset time of this oscillating patterns are different: in Figure.4.12, it does not start until almost the end of the pulse, while in Figure.4.14, it starts 30 milliseconds earlier, which is around the peak magnetic field. This 30 milliseconds determines whether the pulsed magnetic field experiment would be successful or not.

Why there is a 30 millisecond difference? One could start from the probes themselves, since the primary difference the two aforementioned data sets are that we took them using different probes. As a matter of fact, all of our data taken with the straight probe demonstrates the similar pattern, with $\sim$300 Hz oscillation pattern overshadowing signal from the sample. At the same time, not a single shot from Fedro's rotator probe had this issue. As for John's rotator probe, the story is kind of in between. Thus, could it be the case that a probe (with desired quality) will act as a buffer, preventing the noise reaching the cantilever? There are a few traits of a probe that might influence the experiment in this way.

First, the connections between outer shielding tubes and the inner shaft. In an idea situation, the inner shaft of the probe should be connected to its outer shielding tube through probe head, and the two should not be touching each other. Thus, the inner shaft is as if hanging below the probe head, rather than supported by the outer shielding tube. Such a design has one benefit: the noise has to propagate a longer distance (from lower end of outer shielding tube, upto probe head, then down to lower end of inner shaft) before reaching the sample space. The amplitude

of the noise would likely decay due to the distance when it reaches the cantilever. This is the case for Fedor's rotator probe, but not so for the straight probe. As the latter was damaged (inner shaft bent) and was touching outer shielding tube.

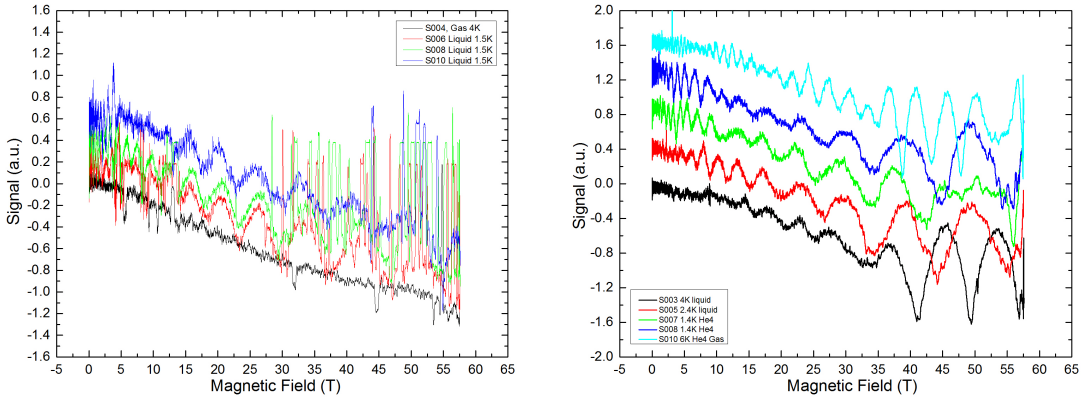

Figure 4.21: signal vs field of $[(Li_{1-x}Fe_x)OH](Fe_{1-y}Li_y)Se$, in Cell-1 magnet with straight probe. Data taken during Aug 2015 trip.

Second, contact between the lower end of probe's inner shaft and the tail of fridge. Due the limited bore size of 60 Tesla short pulse magnet, the fridge has a thin tail with a outer diameter less than 10 millimeter while the lower end of inner shaft has a diameter $\sim$6 millimeter. Thus the lower end of probe's inner shaft and the tail of the fridge are designed to be a tight fit. Should there be any contact between the two parts, one would expect significant amount of noise. Figure.4.21 demonstrates this effect. On the left hand-side, the cantilever was mounted incorrectly, resulting a contact with the fridge's tail, creating huge amounts of spike noises.

Third, the difference between rotator probe and straight probe. The rotator of the rotator probe is mounted by a pair of extremely thin sapphire pins. Compared with the straight probe where cantilever is glued directly onto the lower end of inner shaft, thus having no buffer for noise, the sapphire pins of rotator probe might act as buffer for noise, reducing its amplitude.

Fourth, the structure of probe's inner shaft. Probes in LANL are all handmade by resident researchers, each with a different design. In this case specifically, the straight probe's inner shaft was made of a solid, cylindrical G10 plastic stick, with wiring rapped around its surface. The rotator probe's inner shaft was made of G10 plastic stick with a double crescent cross section, with wiring going through one of the crescent shaped hollow space. In the other hollow space, attached a stainless steel tube as the shaft for rotator's screw. As mentioned above, noise propagating downwards along the inner shaft would experience decaying amplitude, the extend of which might depend on the structure of the inner shaft.

With these in mind, one might settle with the different results obtained using various probes. Particularly, the differences between Figure.4.12 and Figure.4.14 seem to support our claim that Fedro's rotator probe provides better buffer for cantilever. However, if the origin of mechanic noise was as described in Section 4.2.2, then why in Figure.4.14 we have so many noise so early into the pulse?

the Double "Kick"

According to Section 4.2.2, one should expect onset of mechanical noise at end of the pulse. Although it could explain the sudden increase in amplitude at ~90 millisecond in Figure.4.20, it could not explain why all data sets from the straight probe have dominant mechanical noise during most of pulse. To solve this puzzle, one needs to look at the Bdot data in more detail.

Bdot is taken using a coil of wires attached to probe head, with its axis parallel to the magnetic field. In other words, Bdot is the result of electromagnetic induction. Looking at left side panel of Figure.4.22, the Bdot trace crosses zero at the precise moment when magnetic field reaches its peak value; and it has different signs for up and down sweeps. However, the Bdot trace has a extremely sharp peak at the very start of the pulse. This, surprisingly, is due to skin effect of the magnetic

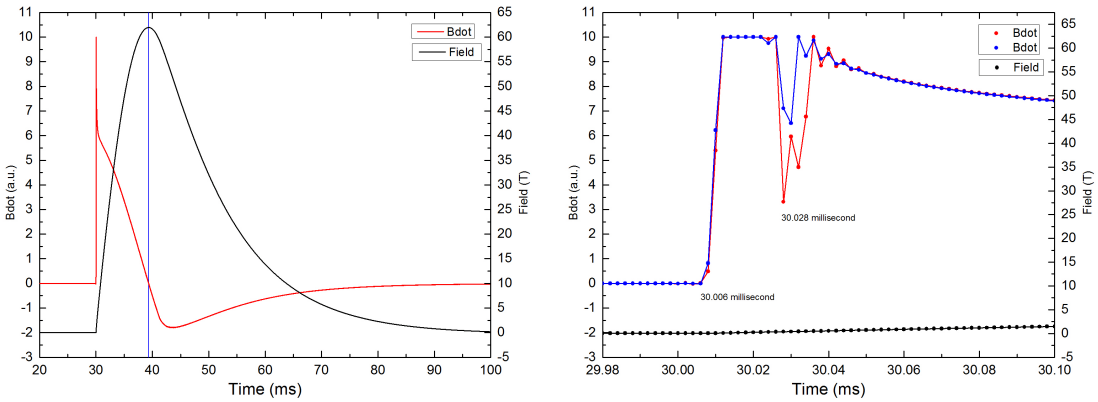

Figure 4.22: Bdot vs Time in Cell-1 magnet with Fedro's rotator probe. Data taken during Aug 2015 trip. Please note that, in the right hand-side plot, the plateau at ∼30.02 millisecond is due to DAQ saturation. Furthermore, DAQ during these shots were working at 500kHz (one data point per 2 microsecond), as represented by each dot in plot.

coils[5]. One could imagine the entire 60 Tesla short pulse facility as a giant LRC circuit. When energy stored at the capacitor bank is released, the current going from the capacitor bank through the magnet coil composes frequencies from a broad spectrum. The high frequency components will go through only the surface of the magnet coil instead of the interior of the metal, resulting in a significantly reduced effective inductance for these components. Thus these high frequency components will go through the magnet much faster while creating a much weaker magnetic field[6] compared with the one created by low frequency components.

Right side panel of Figure.4.22 is a zoom-in of this fast magnetic field induced by the high frequency components. The start of the fast magnetic field (defined as the front of high frequency component) is at 30.006 millisecond. Judging by

[5]Acknowledgments to resident researchers at LANL. I learned about this unexpected fact through discussions with them, during Aug 2015 trip.

[6]Although at this stage I could not observe this fast magnetic field directly, however, in the capacitance channel, there are some suspicious features.

the position of a clear turning point of Bdot trace in Figure.4.23, the end of this fast magnetic field (defined by the front of low frequency component) is at 30.4 millisecond. Since Bdot is still positive at 30.4 millisecond, one could conclude that the low frequency components arrive before the fast magnetic field starting to decay in magnitude. Nonetheless, the speed at which the magnetic field is increasing is changing violently. And we should expect mechanical oscillations induced by the sudden change of stress in magnetic coil. The primary candidate, is the ∼5 kHz oscillating patterns in Figure.4.15. The time elapsed from start of the fast magnetic field to the onset of oscillating patter (at ∼30.994 millisecond) is ∼0.974 millisecond. Assuming an average sould speed of 5000 m/s[7], and assuming an overall distance of ∼5 meters[8], one would get a expected time delay of 1 millisecond, matching our experimental data. This is a very important observation, as it serves as validation to several of our conclusions: the origin of mechanical noise, the way mechanical noise conducted to the cantilever, as well as the following "double kick" argument.

Now that we have realized there are two "kicks" from the magnet: first one as high frequency components setting up at the front of the fast magnetic field and second one as low frequency components setting off towards the end of down sweep. Energy of each kick could be characterized using the strength of magnetic field. In this way, the first kick is weaker than the second one. This explains why both Fedro's rotator probe and straight probe pick up the second kick while only the straight probe picks up the first one, as straight probe is not as a good buffer for noise as Fedro's rotator probe.

[7]Mechanical vibrations need to propagate from the magnet to the fridge, upto probe head then down to sample space, most of which are made of stainless steel and G10 plastic. Sound speed is ∼6000 m/s and ∼3300 m/s for stainless steel and G10 plastic respectively.

[8]The probe is about 2.5 meter long. Connection between probe and fridge is at approximately the middle of outer shielding tube. The magnet is at least 0.5 meter lower than this connection point.

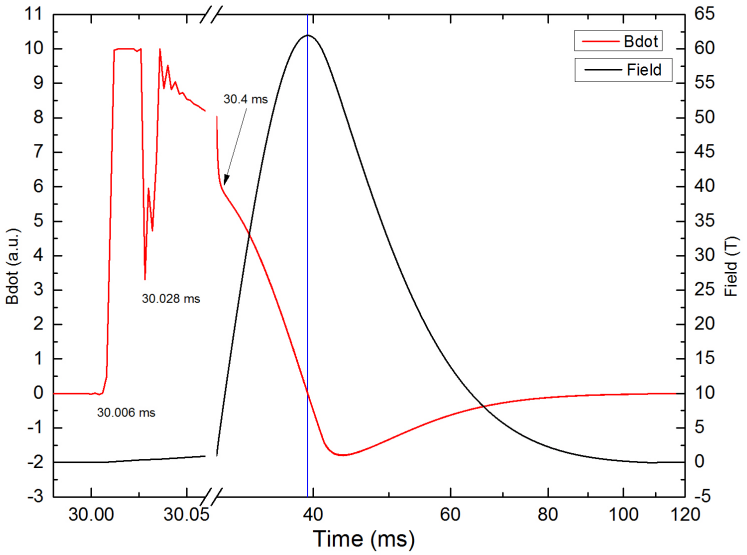

Figure 4.23: Bdot vs Time in Cell-1 magnet with Fedro's rotator probe. Data taken during Aug 2015 trip.

4.2.3 the Singal Retrieval Technique

From previous sections, and Figure.4.17 in particular, we have came to the conclusion that the observed signal is both damped in amplitude as well as delayed in time. The latter effect is more worrying, as the strength of magnetic field is also recorded in time. Thus, if signal from cantilever has a time delay, then any feature we observed from the signal has already had its relation versus magnetic field shifted. In other words, one should never treat the signal from short pulse experiment as in the way one analyzing data from DC magnetic field experiment.

In this section, I will present a method trying to solve this problem. The method depends heavily on computational simulation and iteration of results from said simulation. While this method is reasonably effective for "large" features, it turns out to be less effective for "fine" features on the signal.

the Basic Algorithm

The idea is that, given the parameters of short pulse experiment, and given any "seed" as the "true" signal from sample, the simulation result compared to this "seed" is going to be distorted in the same way that our observed signal compared with sample's true response to magnetic field. Thus, the algorithm has three steps:

Step one, we use the observed signal as "seed", then compared its simulation result with itself, then we will have some information about how signal are distorted.

Step two, we use these information as well as observed data (and its simulation) to recalculate the supposed "true" signal.

Step three, we use the calculated "true" signal as "seed", perform simulation and compare the simulation result with our observed data. If the two matches up, then we have obtained sample's true response to magnetic field. If not, then we will adjust our information about the distortion accordingly, and repeat step two.

Left side panel of Figure.4.24 describes Step one. Here, the blue and orange dots on each traces represents a pair of adjacent data points. From previous sections we know that, at any specific moment, the distortion of signal depends on the speed of sweeping magnetic field as well as sample's response at this particular field strength. Thus, any attempt of finding a global distortion relation for the entire duration of the pulse is doomed to fail. As a matter of fact, such distortion relation has to be found point-wise, for each combination of field profile AND sample's true response. Furthermore, if the time difference between this pair of data points is small enough[9], one could make two assumptions:

[9]For clarity, the plot exaggerated the separation between the pair of data points.

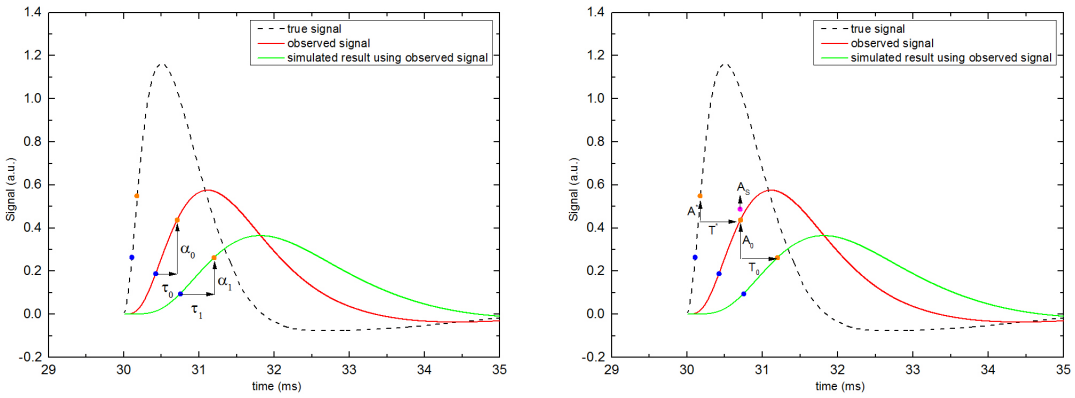

Figure 4.24: Data retrieval algorithm. Dashed black trace is DC field YBCO data interpolated onto pulsed magnetic field, acting as "true signal" from sample. Red trace is simulation result using dashed black trace as "seed", acting as observed signal from pulsed field experiment. Green trace is simulation result using red trace as "seed".

First, one could assume not only that the distortion relation is linear, but also that this linear relation holds for "true" signal versus observed signal as well. Thus we could define a point-wise constant K value:

$$\begin{aligned} K_t &= \tau_0/\tau_1 \\ K_{amp} &= \alpha_0/\alpha 1 \end{aligned} \tag{4.4}$$

Second, the ratio of distortion (K value) not only describes the distortion of a pair of data points belong to the same trace, but also the distortion of each data point between "seed" and simulation result. In other words, on the right side panel of Figure.4.24, we expect that:

$$\begin{aligned} K_t &= T^*/T_0 \\ K_{amp} &= A^*/A_0 \end{aligned} \tag{4.5}$$

T^* is the difference in time of the same data point between sample's "true" response to DC magnetic field and sample's observed response in AC magnetic field, while T_0 is that between observed response and its simulation result.

Obviously, Equation.4.5 is not correct; the distortion will definitely change as observed AC field signal is different from its DC equivalent. Thus we introduce another point-wise variable γ:

$$\begin{aligned} T^* &= \frac{1}{\gamma_t} * K_t * T_0 \\ A^* &= \frac{1}{\gamma_{amp}} * K_{amp} * A_0 \end{aligned} \tag{4.6}$$

This variable γ is the key of our data retrieval simulation. During each iteration, we are trying to approximate the DC field signal by adjusting γ point-wisely. The procedure is as follows:

- perform Step one and obtain the set of K values;
- perform Step two using Equation.4.6, γ values set to 1 for the first time;
- perform Step three, exit if simulation results matches observed signal, otherwise repeats Step two with updated γ;

On the right side panel of Figure.4.24, the magenta dot represents the simulation result of recalculated DC field signal, the equation for calculation γ would be:

$$\gamma_{amp} = \frac{A^*}{A_S} \tag{4.7}$$

Please note that this algorithm is still rudimentary. While it converges rapidly for background baselines, it tends to diverge around sharp features. As a result, this simple algorithm is less effective at retrieving fine features from observed AC field signal.

Simulated Signal Test

Here we use a stretched and interpolated data of YBCO[10] as "seed" to test the effectiveness of the algorithm. The first step is to define all the pairs of data points for comparison, achieved by partitioning the "seed" and its simulated result into four parts, using local maximum(minimum) as boundaries. The second step is to further partition each part of the "seed" evenly in time with step size of 10 microsecond[11], after which one will partition each part of the simulated result into the same numbers of their corresponding parts of the "seed". With this, one could calculate the K values. This process is demonstrated in the left panel of Figure.4.25.

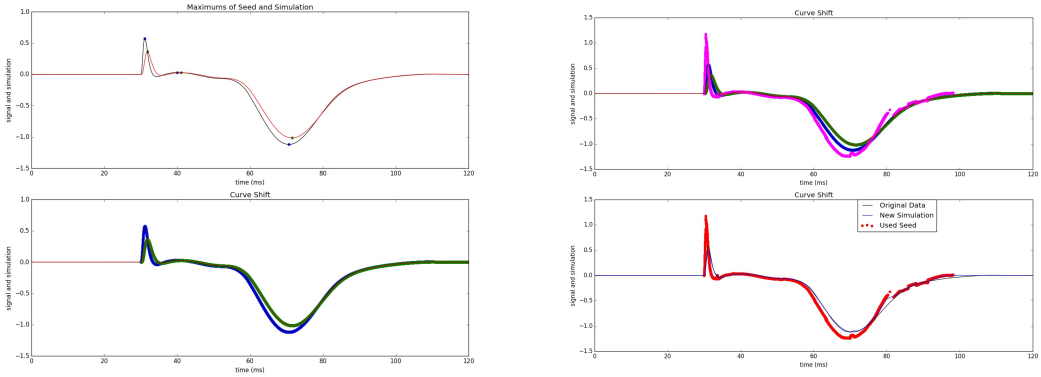

Figure 4.25: Simulation intermediate results.

Once finished the partition process, with calculated K values, one could proceed to Step two and three of the algorithm. This process is shown in the right panel of Figure.4.25. It turns out that for large "back ground" features like hysteresis loop, it took no more than two iteration steps to obtain a good match. However, since this algorithm does not guarantee convergence, too much iterations will over fit the data and the result will diverge. Figure.4.26 displays recalculated DC field signal after

[10] Original data taken at cell-12 of DC facility, NHMFL; original peak field ∼31 Tesla.

[11] Step size of computational simulation of short pulse experiment is 1 microsecond.

two steps of iteration, from which one could see, not only the retrieved hysteresis loop is symmetric, but also in the region above the melting point, original DC field data and the recalculated DC field data matches very well.

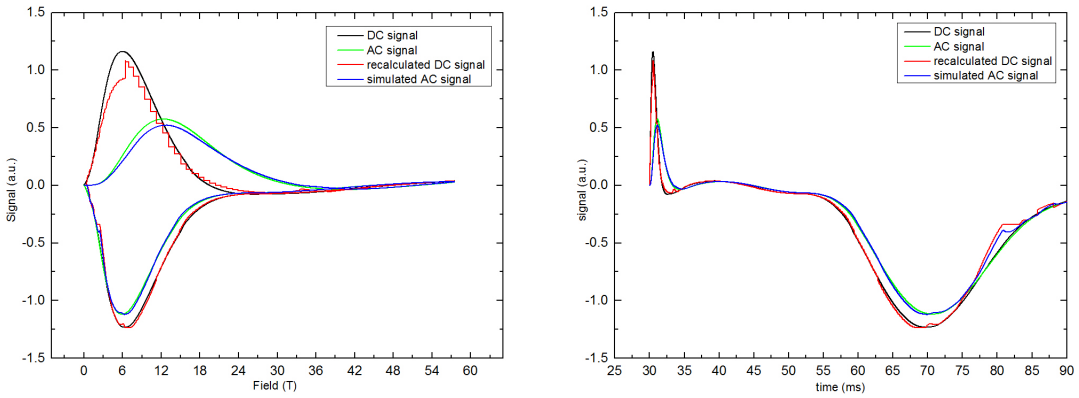

Figure 4.26: Test of data retrieval algorithm. Using stretched and interpolated YBCO data as "seed". This is the result of two step iteration.

However, this algorithm is not without limitations. In addition to its divergence problem, this algorithm tends to amplify noise more so that signal. This is due to the algorithm's inability of distinguishing noise from signal. As a result, the algorithm will try to recreate both. Since noise usually comes with larger $d(signal)/dt$ values, the iteration process will be more sensitive to it than the signal. In the end, any fine features on the observe AC signal will be buried within a thick noise level. This effect is demonstrated in Figure.4.27, where hysteresis loop is retrieved but not the fine features above melting point.

The other limitation of this algorithm, is that, within each section of "seed"(and its simulated result), the algorithm partitions data evenly in time. To start off, there are several reasons why the "seed" has to be partitioned into a few parts using local maximum(minimum).

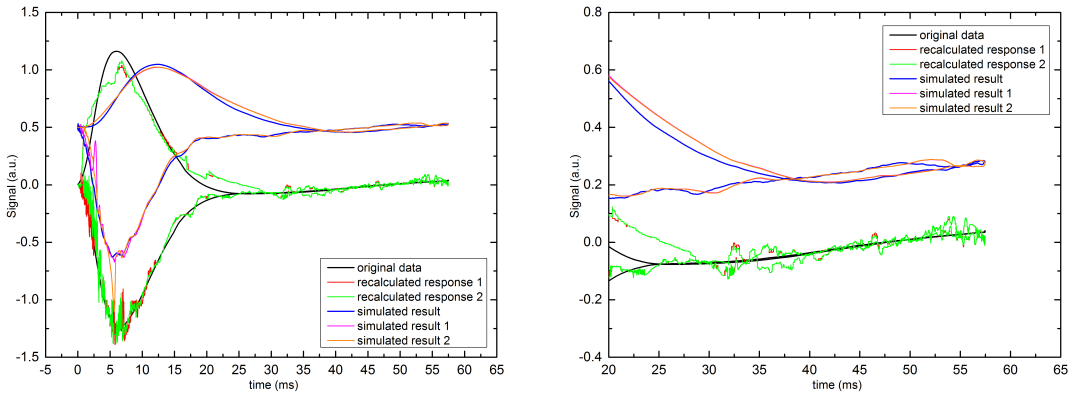

Figure 4.27: Test of data retrieval algorithm. Using stretched and interpolated YBCO data, plus random noise, as "seed".

First, the magnetic field strength, as well as sample's response to magnetic field, is not linear with time. In the right side panel of Figure.4.26, the up sweep hysteresis takes less than 5 milliseconds while the down sweep hysteresis spans more than 20 milliseconds. If one partitions the entire trace evenly in time, then the data point pairs in up sweep is going to be much more sparse than that of down sweep.

Second, since sample's response to magnetic field is not linear, and that there is a time delay between observed AC signal and its simulation result, partitioning the entire trace evenly in time will result in a mismatch of data point pairs. As shown in Figure.4.28, each pair of local maximum(minimum) is connected with blue(green) lines. If partitioning the entire trace evenly in time, these pairs would be mismatched, resulting in the algorithm incorrectly distorting the signal.

However, partitioning the data into 3 or 4 sections, as what we did in Figure.4.26, only solves part of the problem. A good example would be Figure.4.28. Here the first point for partition sections would be the first local minimum at ∼37.5 millisecond. However, the DC field signal have gone through a lot more periods of quantum oscillation by that time point. Thus if one partitions the first 7.5 milliseconds data

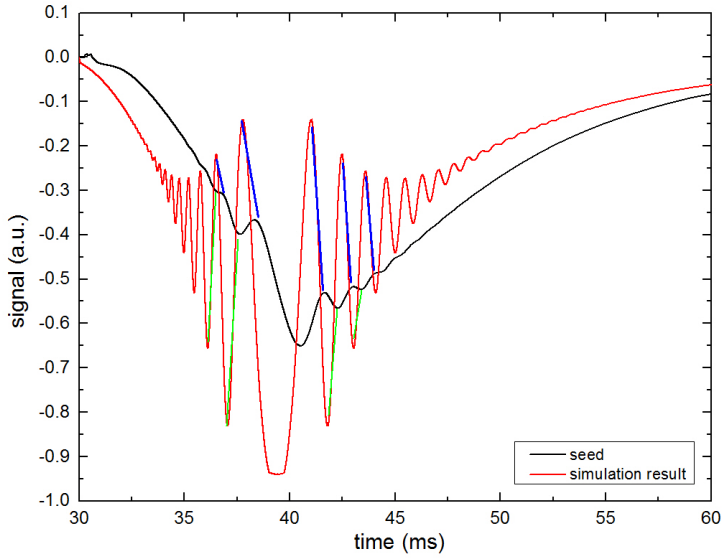

Figure 4.28: Demonstration of fine feature losses during (short) pulsed magnetic field experiment.

evenly, it is likely that data point pairs are going to be mismatched[12]. The demon here is that cantilever's dynamic response to sample's signal, particularly for signals of higher frequency and lower amplitude, is both damped and time delayed. The latter forces us the partition data into separate sections while the former prevents us from finding sufficient boundary points to perform said partition.

[12] On such a clean, artificial data, one could go for 1st or even 2nd order derivative to get finer partition boundaries. However, that would be a luxury facing a real AC field data set.

Chapter 5

Conclusion

In this thesis, we provided conclusive argument to the question: how much does the superconducting state persist into the pseudogap region. This question is important because it is intimate to understanding the picture of competing orders, particularly whether the superconducting state will be wiped out completely by charge ordered state at its onset temperature. Using torque magnetometry, we concluded that the fluctuating superconducting state exists in a very large area above the superconducting dome, overlapping with charge ordered state in the phase diagram, in terms of both temperature and applied magnetic field. Also, a re-examination of previous study indicated a lower estimation of H_{c2} was conducted and corrections to misinterpretations was provided.

Furthermore, we discovered for the first time an abnormality in magnetization above the superconducting dome, in $\sim$15 Tesla (H_k) and below 40 K. This feature is called "kink" feature because it takes the shape of a shallow peak on the differentiated susceptibility curves. The "kink" feature indicates a narrow region where superconducting state weakens rapidly. Compared with higher temperatures (higher than 40 K), with fixed temperature, the superconducting state is stronger than expected below H_k. We linked this feature to results by thermal conductivity, transport, NMR and Xray scattering. We believe this feature is closely related to the onset of charge ordered state.

Finally, a detailed account of our efforts of extending torque magnetometry into pulsed magnetic field experimental conditions is provided. Our preliminary results calls for new torque magnetometry setups with lower Q factor, preferably with new probe design emphasizing mechanical noise isolation. We also identified the need

and offered preliminary methods of reconstructing the time-delayed signal through simulation.

Bibliography

[1] Y. Ando. Electrical resistivity anisotropy from self-organized one dimensionality in high-temperature superconductors. *Phys. Rev. Lett.*, 88:137005, 2002.

[2] J. G. Bednorz and K. A. Muller. Possible high T_c superconductivity in the Ba-La-Cu-O system. *Z. Phys. B: Condens. Matter*, 64, 1986.

[3] R. J. Cava. Bulk superconductivity at 91 K in single-phase oxygen-deficient perovskite $Ba_2YCu_3O_{9-\sigma}$. *Phys. Rev. Lett.*, 58, 1987.

[4] J. Chang. Direct observation of competition between superconductivity and charge density wave order in $YBa_2Cu_3O_{6.67}$. *Nat. Phys.*, 8:871, 2012.

[5] J. Chang. Magnetic field controlled charge density wave coupling in underdoped $YBa_2Cu_3O_{6+x}$. *Nat.Commun.*, 7:11494, 2016.

[6] N. Doiron-Leyraud. Quantum oscillations and the fermi surface in an underdoped high-T_c superconductor. *Nature(London)*, 447:565–568, 2007.

[7] G. Ghiringhelli. Long-range incommensurate charge fluctuations in (Y,Nd)$Ba_2Cu_3O_{6+x}$. *Science*, 337:821, 2012.

[8] G. Grissonnanche. Direct measurement of the upper critical field in cuprate superconductors. *Nat.Commun.*, 5:3280, 2014.

[9] G. Grissonnanche. *arXiv*, 2015.

[10] R. Harris. *Phys. Rev. B*, 74:104508, 2006.

[11] V. Hinkov. Electronic liquid crystal state in the high-temperature superconductor $YBa_2Cu_3O_{6.45}$. *Science*, 319:597, 2008.

[12] M. Hucker. Competing charge, spin and superconducting orders in underdoped $YBa_2Cu_3O_y$. *Phys. Rev. B*, 90:054514, 2014.

[13] C. Jaudet. de Haas-van Alphen oscillations in the underdoped high-temperature superconductor $YBa_2Cu_3O_{6.5}$. *Phys. Rev. Lett.*, 100:187005, 2008.

[14] D. LeBoeuf. Electron pockets in the fermi surface of hole-doped high-T_c superconductors. *Nature(London)*, 450:533, 2007.

[15] D. LeBoeuf. Lifshitz critical point in the cuprate superconductor $YBa_2Cu_3O_y$ from high-field Hall effect measurements. *Phy. Rev. B*, 83, 054506, 2011.

[16] D. LeBoeuf. Thermodynamic phase diagram of static charge order in underdoped $YBa_2Cu_3O_y$. *Nat. Phys.*, 9:79, 2013.

[17] P. A. Lee, N. Nagaosa, and X.-G. Wen. Doping a mott insulator: Physics of high-temperature superconductivity. *Review of Modern Physics*, 78, 2006.

[18] L. Li. Low-temperature vortex liquid in $La_{2-x}Sr_xCuO_4$. *Nat.Phys.*, 3, 2007.

[19] L. Li. Diamagnetism and cooper pairing above T_c in cuprates. *Phy. Rev. B*, 81, 054510, 2010.

[20] D. S. Marshal. *Phys. Rev. Lett.*, 76, 1996.

[21] N. F. Mott. The basis of the electron theory of metals, with special reference to the transition metals. *Proc. Phys. Soc., London, Sect. A*, 62, 1949.

[22] C. Renner. Pseudogap precursor of the superconducting gap in under- and overdoped $Bi_2Sr_2CaCu_2O_{8+\delta}$. *Phys. Rev. Lett.*, 80, 1998.

[23] S. C. Riggs. Heat capacity through the magnetic-field-induced resistive transition in an underdoped high-temperature superconductor. *Nature Physics*, 7:332, 2011.

[24] S. E. Sebastian. A multi-component fermi surface in the vortex state of an underdoped high-T_c superconductor. *Nature(London)*, 454:200, 2008.

[25] H. Shishido. *Phy. Rev. Lett.*, 104:057008, 2010.

[26] C. C. Tsuei and J. R. Kirtley. The pseudogap in high-temperature superconductors: an experimental survey. *Reports on Progress in Physics*, 62, 1999.

[27] I. Vekhter and A. Houghton. Quasiparticle thermal conductivity in the vortex state of high-T_c cuprates. *Phys. Rev. Lett.*, 83, 1999.

[28] B. Vignolle. Quantum oscillations in an overdoped high-T_c superconductor. *Nature(London)*, 455:952, 2008.

[29] A. B. Vorontosov and I. Vekher. Unconventional superconductors under a rotating magnetic field. ii. thermal transport. *Phys. Rev. B*, 75:224502, 2007.

[30] Y. Wang, L. Li, and N. P. Ong. Nernst effect in high-T_c superconductors. *Phys. Rev. B*, 73:024510, 2006.

[31] M. K. Wu and C. W. Chu. Superconductivity at 93 K in a new mixed-phase Y-Ba-Cu-O compound system at ambient pressure. *Phys. Rev. Lett.*, 58, 1987.

[32] T. Wu. Magnetic-field-induced charge-stripe order in the high-temperature superconductor $YBa_2Cu_3O_y$. *Nature*, 477:191–194, 2011.

[33] T. Wu. Emergence of charge order from the vortex state of a high-temperature superconductor. *Nat.Commun.*, 4:2113, 2013.

[34] F. Yu. Magnetic phase diagram of under-doped $YBa_2Cu_3O_y$ inferred from torque magnetization and thermal conductivity. *Proceedings of the National Academy of Sciences*, 113:12667, 2016.